



UNIVERSITAT POLITÈCNICA  
DE CATALUNYA  
BARCELONATECH



Massachusetts Institute of Technology

# Experimental characterization of CMOS photonic devices

Alberto Gómez Gonzalvo

Master's Thesis

*October 2016*

Physical Optics and Electronics Group, Research Laboratory of Electronics

Massachusetts Institute of Technology

Escola Tècnica Superior d'Enginyeria de Telecomunicació de Barcelona

Universitat Politècnica de Catalunya

*Supervised by:*

Prof. Rajeev J. Ram

Prof. José Antonio Lázaro





# Abstract

---

Current electrical interconnects in super-computers and high-performance processors present a bottleneck in terms of bandwidth and power consumption. A migration to the optical domain in order to cope with the connectivity between units (e.g. CPUs and memory) is needed to overcome these issues.

Zero-change CMOS photonic devices represent a very attractive solution to the design of optical on-chip links. This approach makes use of up-to-date CMOS process, having enormous benefits regarding integration with state-of-the-art electronics. Designing and characterizing zero-change CMOS photonic devices is key for the future of optical interconnects.

This thesis presents the characterization both theoretical and experimental of a Silicon-Germanium ring resonator modulator. It represents the first ever depletion modulator up to the date using SiGe as an active material.

Moreover, it shows the best wavelength shift reported so far for zero-change CMOS modulators, enhancing the shift of a pure Silicon device.

The demonstration of this device begins a new era of optical modulator designs using silicon-germanium to enhance modulation efficiency, and therefore reduce power consumption.

# Acknowledgements

---

First of all, I would like to acknowledge Professor Rajeev J. Ram for accepting me in his lab and for guiding me through all this process. All his global vision, his priceless advice and experience have made this research possible.

I would also like to thank Dr. Amir H. Atabaki for helping me in the measurements, theory and for spending countless hours trying to understand the problems we were facing.

Thanks also to all the people in the Physical Optics and Electronics Group: Shayne, Charles, Dinis, Peter, Neerja, Karan, Alyssa, Bill, Gajendra, Gerardo, Jin, Zheng and Gavin. Further thanks to all the friends I made in Boston. You guys made my stay in the USA a lot easier, and made me feel like home.

From UPC-BarcelonaTECH, I would like to acknowledge Professor José Antonio Lázaro. He has co-supervised this work and without him, this dream of being at MIT would have been impossible.

I would not like to forget my beloved group of friends, *Els competitius*, for this awesome journey of 6 years becoming engineers. Gràcies nois.

També voldria agrair tot el suport a una persona molt especial que tot i la distància, no va parar de recolzar-me i enviar-me carinyo.

Y para acabar, me gustaría agradecer todo el apoyo, cariño y confianza que mis padres, hermano y familia han depositado siempre en mí.

This thesis is for all of you.

Alberto

# Summary of original work

---

The following original publications have been reached as a result of the research within this Master's Thesis:

**PAPER 1:** A. Gomez Gonzalvo, A. H. Atabaki, L. Alloatti, R. J. Ram, “SiGe depletion-mode microring modulator in zero-change CMOS”, *In preparation* for Applied Physics Letters.

**PAPER 2:** G. Castanon, D. Cheian, A. Gomez Gonzalvo, A. H. Atabaki, R. J. Ram, “Chirp characterization in microring Si modulators for long-distance silicon-photonics transmission systems”

# Table of contents

---

1	Introduction .....	9
1.1	Thesis outline .....	11
2	Theoretical background .....	12
2.1.1	Drift and diffusion currents .....	13
2.1.2	Types of PN junctions .....	14
2.2	Photonic links .....	15
2.2.1	Optical modulators .....	15
2.2.2	Photodetectors .....	20
3	Device under test .....	23
3.1	Plasma-dispersion enhancement.....	26
3.2	Working principle. Assumptions taken.....	27
4	Experimental results .....	28
4.1	DC measurements.....	28
4.1.1	IV curve.....	30
4.1.2	Free spectral range (FSR).....	30
4.1.3	Resonance parameters .....	31
4.1.4	Wavelength shift.....	33
4.2	Frequency measurements .....	34
4.3	Eye diagram.....	37
4.3.1	Asymmetry of the eye diagram .....	39
5	Conclusion.....	40
5.1	Future work .....	41
6	Appendix .....	42
6.1	Transmission derivation in an optical ring resonator .....	42
6.2	Theoretical derivation of Soref's Equations.....	45
6.3	Optimization of the light incident angle.....	47



# Acronyms

---

ASE	Amplified Spontaneous Emission
CMOS	Complementary-Metal-Oxide-Semiconductor
CPU	Central Processing Unit
DC	Direct Current
DSL	Digital Subscriber Line
ER	Extinction Ratio
FSR	Free Spectral Range
FWHM	Full-Width Half Maximum
GC	Grating Coupler
GS	Ground Signal
IL	Insertion Loss
MZI	Mach-Zehnder Interferometer
OSC	Oscilloscope
PD	Photodiode
QE	Quantum Efficiency
RRM	Ring Resonator Modulator
RX	Receive side
SiGe	Silicon-Germanium
SOA	Semiconductor Optical Amplifier
SSMF	Standard Single Mode Fiber
TX	Transmit side
VNA	Vector Network Analyzer
WDM	Wavelength Division Multiplexing



# 1 Introduction

Optical networks have become the standard for long-haul communications, replacing electrical wires, due to their increased bandwidth with respect to conventional Digital Subscriber Line (DSL) systems. Inside processing machines, such as microprocessors, electrical wires still dominate short-distance communications.

The interconnection between different units in a microprocessor (e.g. CPUs with I/O or with memory) experience now a limitation in terms of bandwidth [1-2]. A bottleneck in terms of speed and power consumption exists in interconnection conventional systems [3]; electrical wires lose energy and reduce the communication speed. The high density in the current interconnect networks leads to increased crosstalk and decreased bandwidth.

The main potential of the CPU is not used because of the bottleneck in the electrical interconnects. [4] shows a microprocessor with only about one half of the full CPU capacity used due to the limitation of metal interconnects.

A full transition to the optical domain will overcome this limitations [5]. The term “silicon photonics” arises from the fact that silicon is the main material of Complementary-Metal-Oxide-Semiconductor technology (CMOS). Integration of photonic components with this technology is key for making optoelectronic devices with high performance and reduced power consumption.

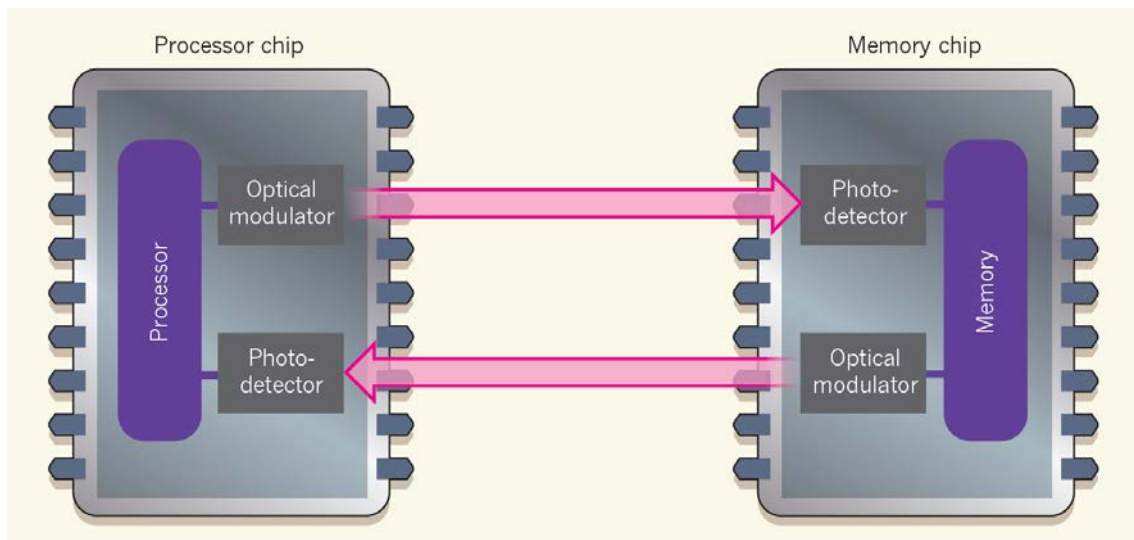


**Figure 1.1. Architecture of an electro-optical microprocessor.** The system integrates electronic components (purple) and photonic ones (grey). The data travels along an optical fiber (pink) [3].

Some of the demonstrated so far optical modulators are manufactured using materials such as III-V elements (e.g. InGaAsP heterojunctions), that have benefits for single devices, such as increased electron and hole mobility. However, when thinking about the integration with electronics at large scale, these materials become problematic. They require manufacturing with very expensive custom processes.

Another approach is to use CMOS-compatible processes [6-8], modifying an old CMOS process. If the target is the modern processing units, the use of old custom CMOS process is not desirable. This leads at the end to a custom CMOS process, so also an expensive process.

These proposed solutions would require a multichip approach, in which the photonics and the electronics are manufactured independently, using different processes.

The approach followed here is known as “zero-change CMOS”. This technique uses existing up to date commercial CMOS processes, designing the photonics and the electronics with any extra process. This allows the possibility of integration with state-of-the-art transistors at large scale with CMOS high yield (higher than 99% [9]). Moreover, the cost associated to photonics manufacturing would be much smaller to the cost of a multichip approach.

However, working with CMOS processes comes with lots of limitations in terms of design. The number of metal layers is restricted, the depth of implants is fixed, the doping cannot be controlled with precision, etc. This makes, for example, vertical PN junctions not feasible in zero-change CMOS devices.

Several demonstrations of single devices (modulators, detectors) have been reported using this approach [10, 11].

[12], recently reported in *Nature*, shows the first ever demonstration of an electro-optical microprocessor using a photonic link to make the interconnection between the memory and the CPU.

It integrates 70 million transistors and 850 photonic components. Although the data rate achieved of 2.5 Gbps is slow compared to state-of-the-art microprocessors, this demonstration could represent a new era of photonic interconnects in microprocessors, enabling high-performance computers with reduced power consumption and without interconnect speed limitations.

In this thesis we will assess the performance of a silicon-germanium (SiGe) modulator, demonstrating for the first time a depletion modulator using SiGe as an active material. This device has the particularity that it has been already reported [13] working as a photodetector. Future device developments with this idea of having a detector that at the same time is a modulator, could reduce the number of optical links need for on-chip communications.

## **1.1 Thesis outline**

The remainder of the report is organized as follows:

Chapter 2 is devoted to the theoretical explanation of the working principle of ring resonators as well as detectors, starting from a basic PN junction perspective.

Chapter 3 talks specifically of the device we are testing: the first ever SiGe ring resonator modulator. We will explain its working principle and the main benefits of using SiGe as an active material.

Chapter 4 presents the experimental results and the setup used for the experiments.

Finally, in Chapter 5, the conclusions of the thesis are summarized and the future work is presented.

# 2 Theoretical background

## 2.1 PN junction. Basic operation

The union of a P-type semiconductor, with a massive concentration of acceptors, with density  $N_A$ , and a N-type semiconductor, with donor concentration  $N_D$ , creates a PN junction.

Under equilibrium conditions, (no voltage applied to the junction), and in contact, the electrons from the N region will diffuse to the P region, where there is a smaller concentration of electrons. The same will happen with holes diffusing from the P region to the N region. This will leave a net charge behind, that will create an electric field on the other direction that will prevent total diffusion the carriers at both sides.

The region at which there is the net charge with the opposite dopant is called the depletion layer. The width of the depletion layer is called the depletion width  $W$ . In thermal equilibrium the expression in Equation (2.1) can be obtained:

$$W = \sqrt{\frac{2\varepsilon\phi_{built}}{q} \frac{N_A + N_D}{N_A N_D}} \quad (2.1)$$

where  $\phi_{built}$  is the built-in potential of the junction in equilibrium.

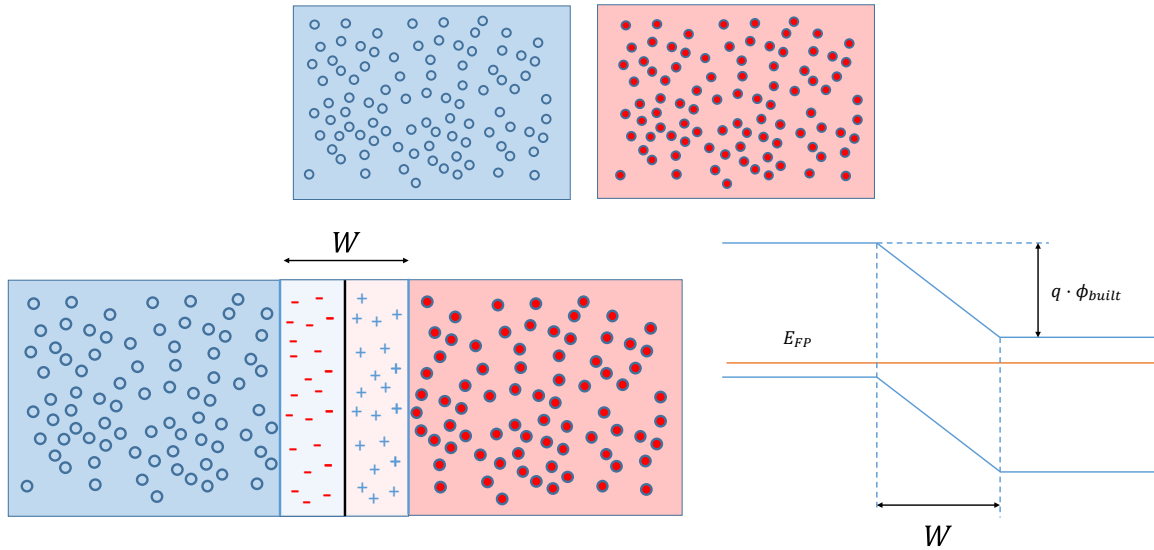


**Figure 2.1: Top: P (blue) and N (red) semiconductors before their contact. P has a massive concentration of holes (blue circle) and N has a massive concentration of electrons (red circle). Bottom left: PN junction after the contact, in equilibrium. Charges are left behind due to the diffusion of carriers, creating a depletion width  $W$ . Bottom right: Band diagram of the PN junction in equilibrium. There is an energy barrier  $q \cdot \Phi_{built}$  between the P and the N region.**

When we apply a forward bias voltage  $V_b$  to the terminals of the junction, the barrier between both sides of the junction diminishes and therefore diffusion is easier to happen.

$$W = \sqrt{\frac{2\varepsilon(\phi_{built} - V_b)}{q} \frac{N_A + N_D}{N_A N_D}} \quad (2.2)$$

On the other hand, if we apply a reverse bias, the energy barrier grows.

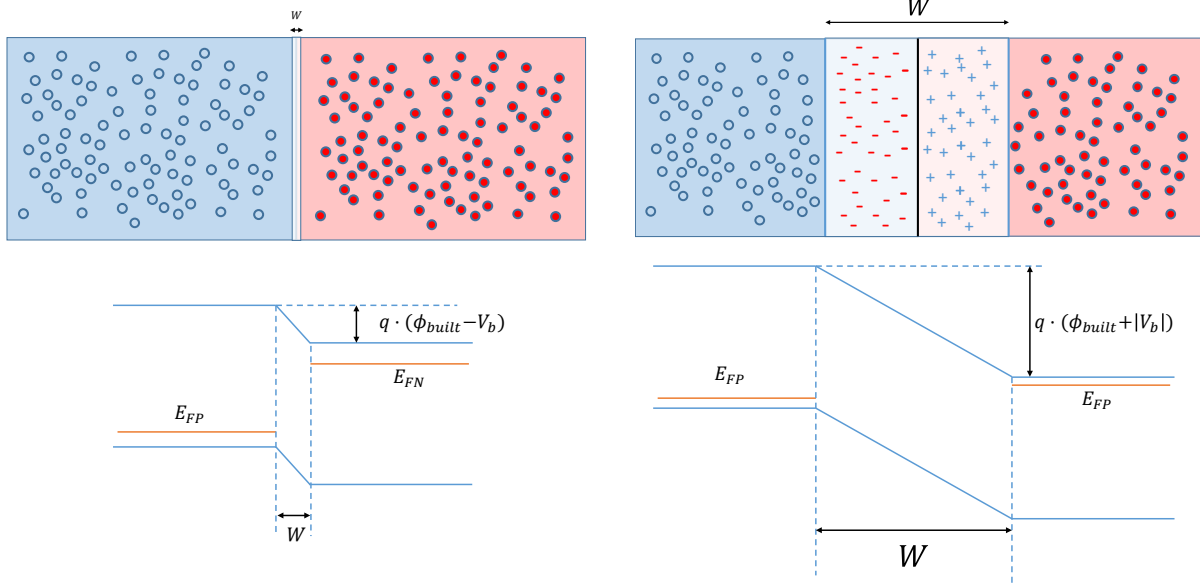


**Figure 2.2: Left: PN junction under forward bias, with reduced energy barrier and smaller  $W$ .**

**Right: PN junction with reverse bias conditions, bigger  $W$ .**  $E_{FP}$ : Pseudo Fermi level of P semiconductor,  $E_{FN}$ : Pseudo Fermi level of N semiconductor,  $W$ : depletion width of the PN junction,  $\phi_{built}$ : built-in potential,  $V_b$ : bias voltage at the terminals of the PN junction.

### 2.1.1 Drift and diffusion currents

When the PN junction is in equilibrium, the diffusion current and the drift current created by the net charges left behind are compensated by each other.

Applying a forward bias to the junction will diminish the barrier  $q(\phi_{built} - V_b)$  and therefore diffusion will happen easier, having an increased diffusion current. The mobility of the electrons and holes will be then dominated by diffusion current.

On the other hand, applying a reverse bias to the junction will increase the barrier  $q(\phi_{built} + |V_b|)$  and therefore the energy barrier for diffusing will be higher. The drift current will increase, preventing the carriers to diffuse, being the main driving force for the carriers.

Biasing the junction with a small forward bias is beneficial in terms of achieving more change in the depletion width than applying reverse bias.

Regarding the speed, drift of carriers is an extremely fast mechanism whereas diffusion is slower. Therefore, biasing the junction with reverse bias is beneficial in terms of speed.

### 2.1.2 Types of PN junctions

We have to take into account that the requirements of the device we are going to work: a ring resonator device that is completely made under zero-change CMOS technology.

For creating ring devices, people have used mainly three types of junction: the lateral junction, the vertical junction and the interleaved junction. The design of the PN junction is key to the performance of the device; designing a good junction can lead to have great performance in terms of resistance and capacitance, that will lead to excellent speed and Extinction Ratio (ER) of the device.

We have to note that the main factor contributing to the bandwidth of the device is the  $RC$  product, contributing to the delay of the carriers reaching the depletion region. The  $RC$  constant directly sets the 3 dB bandwidth of the device.

Intuitively, the smaller is the distance the carriers need to travel before they reach the depletion region, the smaller is the resistance and therefore bigger the 3 dB bandwidth. This is the idea behind a vertical junction. However, vertical junction is not feasible in zero-change CMOS technology. This is because of the limitation of the depths of the implants in CMOS process. In modified CMOS processes it is possible to make such junction with heavily doped materials, being able to benefit of the increased bandwidth (e.g. the work done in [7]).

In Figure 2.3 we can observe the three types of junction with theoretical calculations of the frequency behavior of the device.

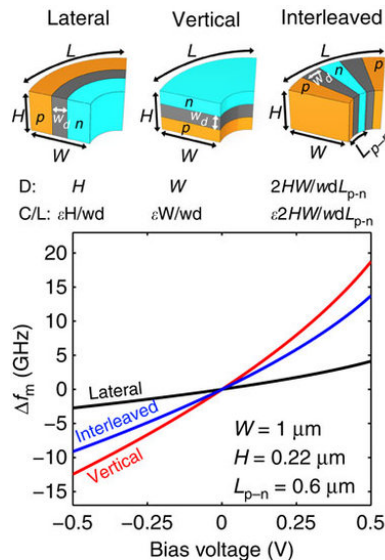


**Figure 2.3: Types of PN junctions and their frequency performance vs bias voltage [7].**

The use of interleaved junctions tries to overcome the high distance that need to travel the carriers in the lateral junction. This is then the approach to follow when working with zero-change CMOS, as vertical junctions are not feasible.

## 2.2 Photonic links

When we are talking about any communication link, we should differentiate three different elements: the transmitting side (TX), the transmission media and the receiving side (RX). In photonic links, the TX device is an optical modulator, the transmission media is an optical fiber/waveguide and the RX device is a photodetector.

The optical modulator acts as a hub that converts the electrical information generated by the electrical source (usually logical 1's and 0's) to two optical power levels.

The transmission media is usually a waveguide or optical fiber. When talking about supercomputers and in - data center applications, the transmission media is a short optical fiber – no more than 100 m long. In [12] the round trip distance of the photonic full-duplex link was 20m.

The photodetector converts the optical information from the optical to the electrical domain. The electronics after the photodetector will translate this electrical information to logical bits.

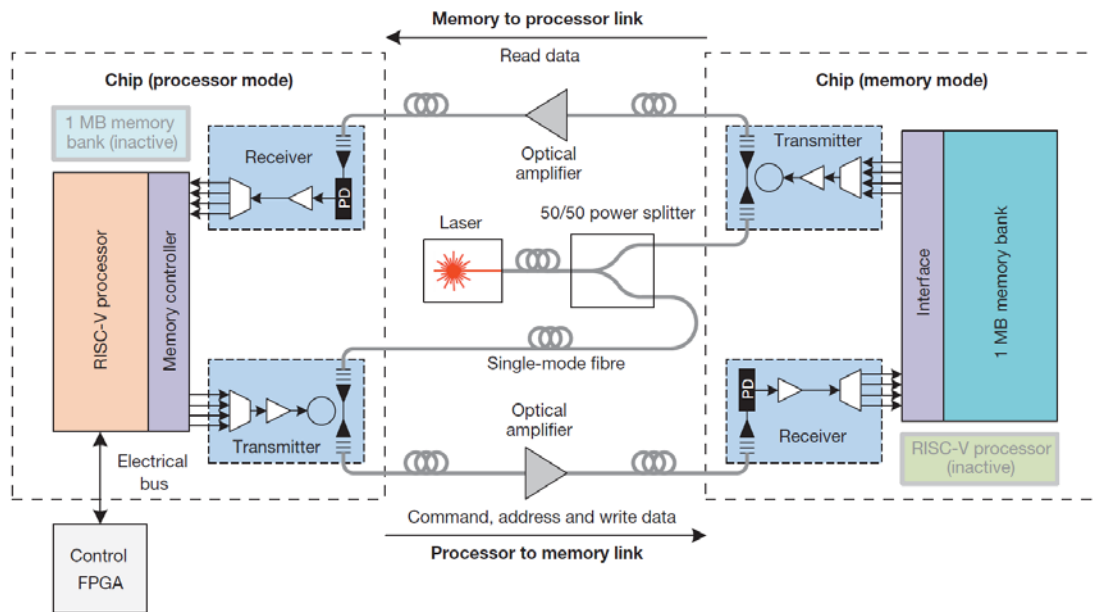


**Figure 2.4: Photonic link (grey) in a microprocessor architecture [12].** It incorporates modulator and detector in each of the sides. The transmission media is a Standard Single Mode Fiber (SSMF).

### 2.2.1 Optical modulators

The main goal of an optical modulator in a photonic link is to convert the information from electrical bits to optical power levels. When varying the voltage or current in the terminals of the device, the modulator should be able to output different optical power levels.

There are two types of optical modulators: Mach-Zehnder Interferometer (MZI) and the Optical Ring resonator.

The working principle of a MZI is the following: when we modulate the phase of the light in the two different arms, constructive and destructive interferences are created. Then, when the light at both arms is added, we observe the output, result of this interference.

If an unbalanced configuration is chosen, one of the arms has to travel a significant distance in order to acquire a  $\pi$  phase difference with respect to the other arm. Thus, a big area is needed in order to satisfy this requirement. This represents a restriction in terms of their utility in interconnection purposes in a microprocessor.

Moreover, the large size is not the only issue. The voltage needed in order to obtain a good Extinction Ratio (ER) in the State-of-the-Art Silicon modulators is above 6 Volts (V) [14-15]. The high driving voltage needed for the modulation makes the power consumption increase dramatically, since  $P \propto V^2$ . This value will be noticeably reduced in optical ring modulators.

The combination of these two drawbacks, size and power consumption, make MZI not a good approach for the next generation on-chip photonic interconnects.

### 2.2.1.1 Optical ring modulator

The working principle of an optical ring modulator will be explained in detail, since it is the one modeled, characterized and tested in our experimental work.

The structure of the modulator has two parts: an optical waveguide and a ring, that is the resonant device.

When the light travels through the waveguide, some fraction of the light is coupled into the modulator. After travelling inside the modulator, some fraction of this light is coupled again out to the waveguide. The interference between the wave directly transmitted through the waveguide and the one that coupled out of the ring determines the output power value.

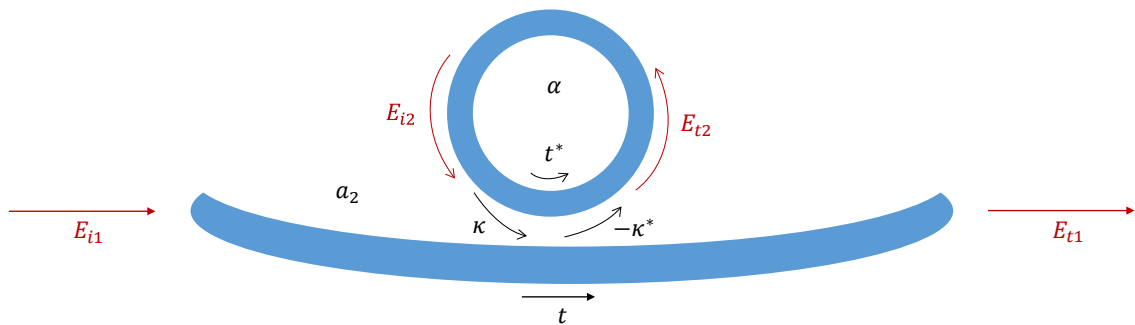


**Figure 2.5: Optical ring resonator modulator diagram.** It incorporates a waveguide and a ring resonator structure that contains the PN junction.



The relation between the input and output waves can be thought as a two-port circuit:

$$\begin{bmatrix} E_{t1} \\ E_{t2} \end{bmatrix} = \begin{bmatrix} t & \kappa \\ -\kappa^* & t^* \end{bmatrix} \cdot \begin{bmatrix} E_{i1} \\ E_{i2} \end{bmatrix} \quad (2.3)$$

Where  $E$  denotes the normalized amplitude of the mode,  $|E|^2$  would be the modal power.  $t$  is the transmittance, and  $\kappa$  is the coupling coefficient between the waveguide and the ring.  $\alpha$  is the loss coefficient of the ring.

A closed expression for the transmitted power can be derived [16]:

$$P_{t1} = |E_{t1}|^2 = \frac{\alpha^2 + |t|^2 - 2\alpha|t|\cos(4\pi^2 n \frac{r}{\lambda} + \varphi_t)}{1 + \alpha^2|t|^2 - 2\alpha|t|\cos(4\pi^2 n \frac{r}{\lambda} + \varphi_t)} \quad (2.4)$$

Where  $\varphi_t$  is the phase of the coupler,  $r$  the radius of the ring,  $\lambda$  the wavelength of the wave and  $n$  is the effective refractive index of the modulator.

The shape of this transmission curve follows a Lorentzian expression. The wavelength at which the transmission minimum is reached is called the resonance wavelength. This will be reached when the output of the cosine (in Eq (2.4)) is maximum, having then the minimum possible of the transmitted power:

$$P_{t1res} = |E_{t1}|^2 = \frac{\alpha^2 + |t|^2 - 2\alpha|t|}{1 + \alpha^2|t|^2 - 2\alpha|t|} = \frac{(\alpha - |t|)^2}{(1 - \alpha|t|)^2} \quad (2.5)$$

Therefore, photonic engineers' goal is to design modulators with  $\alpha = |t|$ , in order to have a real minimum in transmission. This is known as critically-coupling condition.

When we apply a voltage to the terminals of the PN junction, this changes the depletion width of the device. As stated in (2.2):

$$W = \sqrt{\frac{2\varepsilon(\phi_{built} - V_b)}{q} \frac{N_A + N_D}{N_A N_D}} \quad (2.2)$$

The depletion width changes when applying a bias voltage to the PN junction. The change in the depletion width makes carriers diffuse and drift, and the concentration of carriers changes. When we reverse bias, the depletion region is wider, and therefore this voltage depletes the ring from free carriers. On the other hand, if we apply a small forward bias the carriers are refilled by diffusion.

A change in the carrier concentration, affects the refractive index of the ring, due to the plasma-dispersion effect. This change of the refractive index was initially explained by the Drude model, but was experimentally characterized by Soref *et al.* [17]. In silicon the change in the refractive index follows the expression:

$$\Delta n_{electron} = -1.1 \times 10^{-4} \left( \frac{N_{electron}}{2 \times 10^{17} cm^{-3}} \right)^{1.045} \left( \frac{\lambda}{1.3 \mu m} \right)^2 \quad (2.6)$$

$$\Delta n_{hole} = -2.3 \times 10^{-4} \left( \frac{N_{hole}}{1 \times 10^{17} cm^{-3}} \right)^{1.045} \left( \frac{\lambda}{1.3 \mu m} \right)^2 \quad (2.7)$$

Where  $N_{electron}$  and  $N_{hole}$  represent the density change in carriers in electrons and holes, respectively, and  $\lambda$  is the operating wavelength. These equations will be explained afterwards, since the particularity of our device is that we achieve a higher  $\Delta n$  than the state-of-the-art Si devices.

From Eq. (2.4) we can extract that a change in refractive index will directly affect the transmission curve. Since all the variables inside the cosine are constant, the change in the refractive index will shift the resonance peak (the  $\lambda$  at which the minimum is reached will shift).

To sum up, the work flow of a micro ring resonator modulator is:

- The bias voltage applied changes the depletion width of the PN junction.
- The change in the depletion region comes by a change in the concentration of electrons and holes.
- A change in the concentration leads to a change in the refractive index (Soref's equations).
- A change in the refractive index shifts the resonance peak.
- Putting the laser in between both transmission curves will generate two different optical power levels, converting then from the electrical to the optical domain.

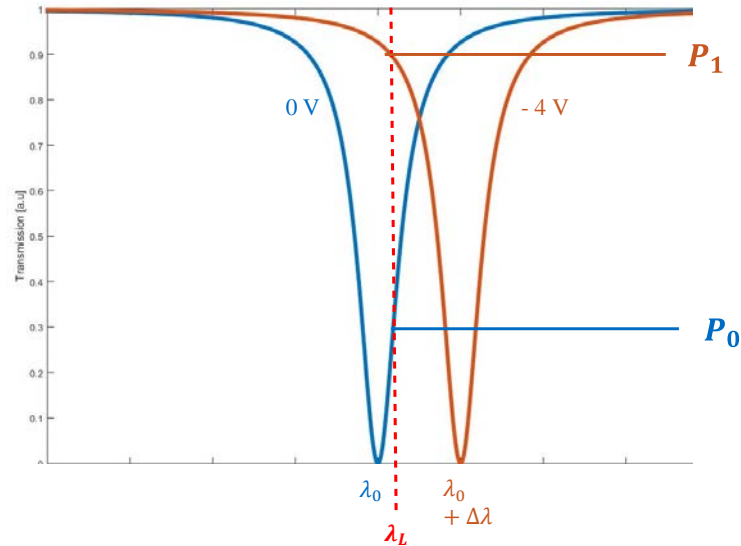


**Figure 2.6: Working principle of a ring resonator modulator.** The transmission curve shifts when applying voltage due to the plasma-dispersion effect, that makes a change in the refractive index. If we put the wavelength of our laser in a middle point, we will generate two optical power levels.

## Overcoupling, undercoupling and critical coupling

In Eq. (2.5) we have shown that the minimum power is reached at the resonance wavelength:

$$P_{t1_{res}} = \frac{(\alpha - |t|)^2}{(1 - \alpha|t|)^2} \quad (2.5)$$

The values of  $\alpha$  and  $t$  will determine whether the ring is undercoupled, critically coupled or overcoupled. For understanding better the behavior of the ring in every condition, we use the equation obtained in Section 6.1:

$$\frac{a_o}{a_i} = \frac{\frac{1}{2} \left( \frac{1}{Q_i} - \frac{1}{Q_c} \right) - j \frac{\Delta\omega}{\omega}}{\frac{1}{2} \left( \frac{1}{Q_i} + \frac{1}{Q_c} \right) - j \frac{\Delta\omega}{\omega}} \quad (2.8)$$

$Q_c$  is the coupling quality factor, which is related to the fraction of light that goes from the waveguide to the ring and from the ring to the waveguide. It is inversely proportional to the coupling loss,  $\gamma_c$ . Therefore,  $1/Q_c \propto \gamma_c$ .

On the other hand,  $Q_i$ , the intrinsic  $Q$ , is related to the amount of loss inside the ring. A lossless ring would have a  $Q_i = \infty$ . The intrinsic  $Q$  is related to the loss factor inside the ring,  $\gamma_i$ .

At resonance,  $\Delta\omega = 0$ , therefore, the expression for the transmission curve will be

$$\frac{a_o}{a_i} = \frac{\frac{1}{Q_i} - \frac{1}{Q_c}}{\frac{1}{Q_i} + \frac{1}{Q_c}} \quad (2.9)$$

The critically coupling condition is reached when the intrinsic and coupling loss factors are the same. Therefore, when  $\gamma_i = \gamma_c \rightarrow \frac{1}{Q_i} = \frac{1}{Q_c}$ . This is the only condition that gives us a null in the transmission curve. This is the best possible design for a modulator.

The condition for undercoupling is  $\frac{1}{Q_i} < \frac{1}{Q_c}$ , that means that the coupling loss is bigger than the intrinsic loss. The modulator is overcoupled if  $\frac{1}{Q_i} > \frac{1}{Q_c}$ .

Experimentally, it is impossible to get a 100% critically coupled resonator. However, playing with the power of the input signal, we can change the amount of recombinations that take part inside the ring, and therefore change the intrinsic  $Q$ . In that way, we can determine whether we are undercoupled and overcoupled and try to go as close as possible to the critical coupling condition.

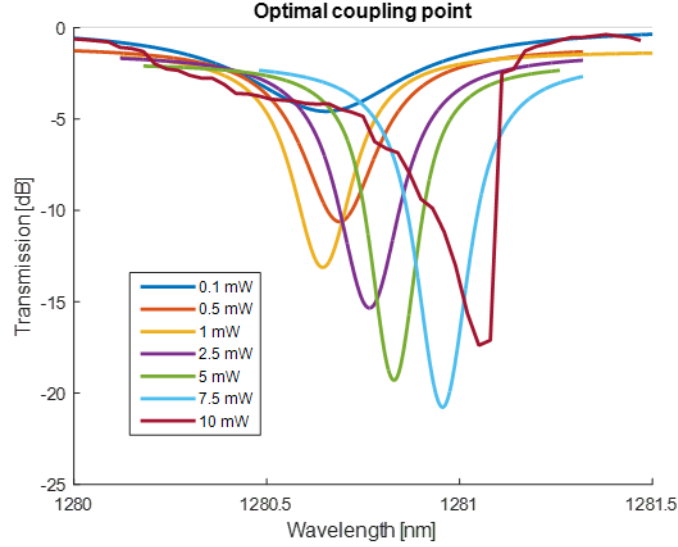


**Figure 2.7: Transmission curves (fitted data except for 10 mW) with different input power conditions.** The device shows undercoupling for  $P < 5$  mW and overcoupling for  $P = 10$  mW.

Figure 2.7 shows experimental data with our SiGe modulator. We can observe that as we increase the input power the extinction gets better. This is because as we increase the power, the number of recombinations that happen inside the ring increases. Therefore the intrinsic loss of the ring,  $\gamma_i$ , increases and the numerator term  $\frac{1}{Q_i}$  increases, too. There is an optimal point in which  $\frac{1}{Q_i}$  matches  $\frac{1}{Q_c}$ . In our case that point is 7.5 mW. Going further to that point makes the ring overcoupled, having too much intrinsic loss compared to the coupling one.

### 2.2.2 Photodetectors

Photodiodes, also known as photodetectors, are the RX device in a photonic link. Photodiodes convert the incident optical radiation to an electrical signal, either voltage or current. They convert optical power levels to electrical bits.

The mechanism behind its working principle is the photon absorption. An incident photon with enough energy is absorbed by an electron from the valence band. Once it has acquired the energy of the photon, this electron jumps to the conduction band. The result is the creation of an electron-hole pair.

In order to benefit photogeneration, a PN junction should be reversed bias. In this way, the drift current is dominant. Therefore, electron and hole pairs created due to the photon absorption go fast to the N and P regions, respectively (see Section 2.1.1).

There are several ways of designing a photodetector. The most straightforward one is to place the photodetector sensing part directly into the input waveguide. In that way, the light

comes into the detector and generates current. The electronics after the detector decide the logical bit value of the input signal depending on the generated current level.

Another possible design for photodetectors is a ring resonator device. The main working principle is to place a ring resonator close to the input waveguide. If the light is in the appropriate wavelength, it will be coupled into the detector and it will get absorbed there.

For understanding better the benefit of having a ring resonator in detection, we have to take into account the resonance condition:  $\beta l = 2\pi m$ , where  $m$  is an integer value. If the light is in the resonant wavelength, the wave that comes on the end part of the ring will be in phase to the light that is coupled into the ring. In that way, more amount of light will travel inside the ring waiting to be absorbed.

We can have an analogy with a Fabry-Perot device. We can think about a ring resonator as two mirrors. One mirror represents the coupling from the waveguide to the ring and vice versa, and the other mirror represents the amount of light that goes into the ring and reaches the output port. For making it easier, we will think that the ring is lossless, i.e. all the light that comes into the ring goes either again into the ring or is coupled outside. Therefore, we will think about the output mirror as a perfect reflector.

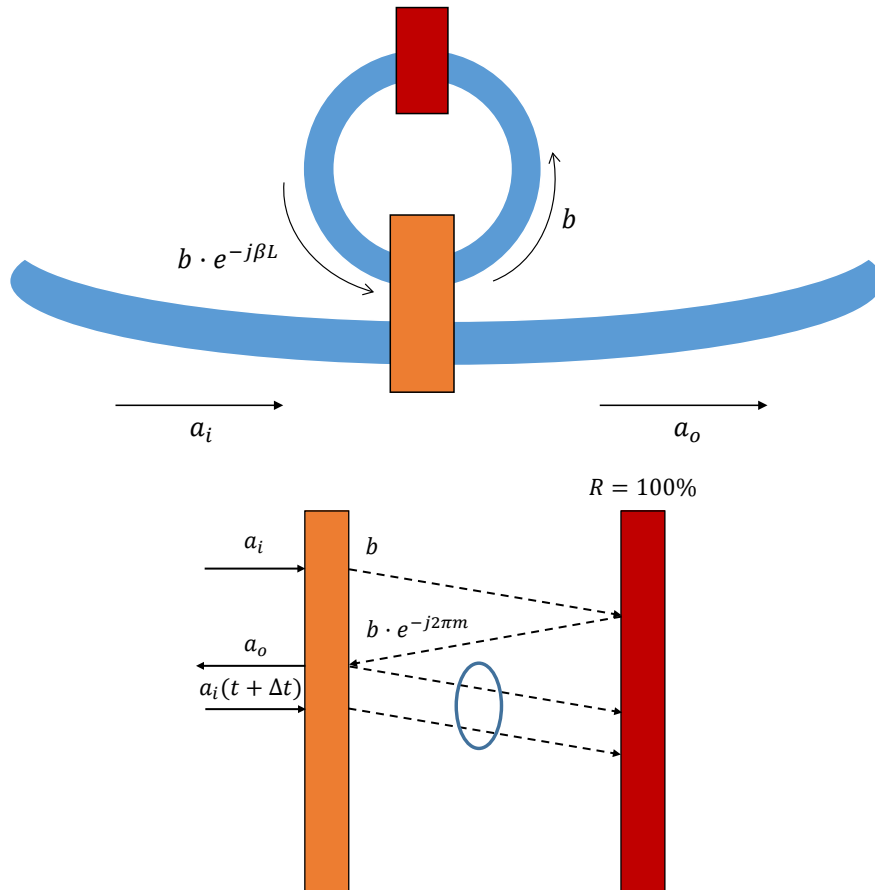


**Figure 2.8: Top: Ring modulator. Bottom: Analogous Fabry-Perot explanation.** The in-phase light makes constructive interference and therefore increased responsivity is achieved.

In the time instant  $t$ , a wave  $a_i$  goes into the input waveguide, and a fraction of this wave is coupled inside the ring. At time  $t + \Delta t$ , where  $\Delta t$  is the time that takes the wave to do a complete turn, a fraction of this turn will go again into the ring. This will interfere constructively with the input wave  $b(t + \Delta t)$  and therefore the amount of light inside the detector will be amplified.

This mechanism makes that the light circulates inside the ring until it gets absorbed, generating more photocurrent. It is very important to notice that the benefit of the ring detector is only valid at the resonance wavelength of the ring. Otherwise, the interference between waves will be destructive and therefore the responsivity will decrease.

# 3 Device under test

---

The device that we have tested is a Silicon-Germanium ring resonator detector [13]. It was already reported working as the RX of a photonic link, showing 0.55 A/W responsivity at 1180 nm operating wavelength. The device was manufactured under zero-change CMOS (Global Foundries/IBM 45 nm SOI process). Our goal is to test this device as a modulator, not a detector.

The device is a ring-resonator detector, with interleaved PN junctions with an access waveguide that couples the light into the ring. In order to couple the light from the outside to the waveguide, Grating Couplers (GC) are used. The structure makes use of the resonance of the ring to enhance the responsivity, as we explained in Section 2.2.2.

Several devices were tested. The main difference between them is the distance between the waveguide and the ring. Several gaps were chosen, ranging from 170 nm to 290 nm. The reason for that is an easy way to change the coupling coefficient between different devices, in order to find the best resonator experimentally.

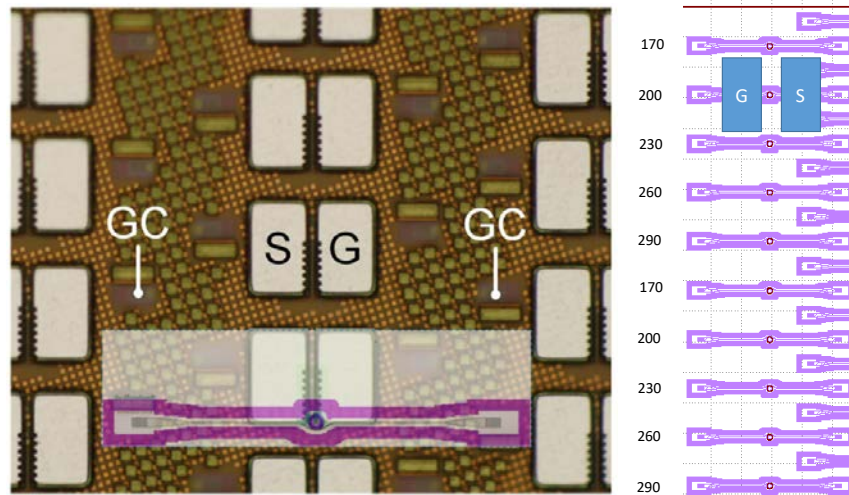


**Figure 3.1:** Left: Microscopic image of the physical layout (purple highlight is the detector). The grating couplers (GC) allow the light to be coupled into the ring. The Signal (S) and Ground (G) electrical pads allow to put the probe to sense the converted electrical signal [13].

**Right:** Schematic of the different devices. The number in the left shows the distance in nm between the waveguide and the ring.

The ring radius for all the devices is 5  $\mu\text{m}$ . Inside the interleaved PN-junction cavity, a SiGe 500 nm wide ring is etched. The SiGe percentage is estimated to be  $\text{Si}_{0.7}\text{Ge}_{0.3}$  [18]. This SiGe ring makes a crucial benefit when using the ring as a detector. We will see in Section 3.1 the benefits of having a silicon-germanium pocket when using the resonator as a modulator. SiGe is traditionally used in electronic transistor design (45 nm CMOS) in order to stress the p-FET channels.

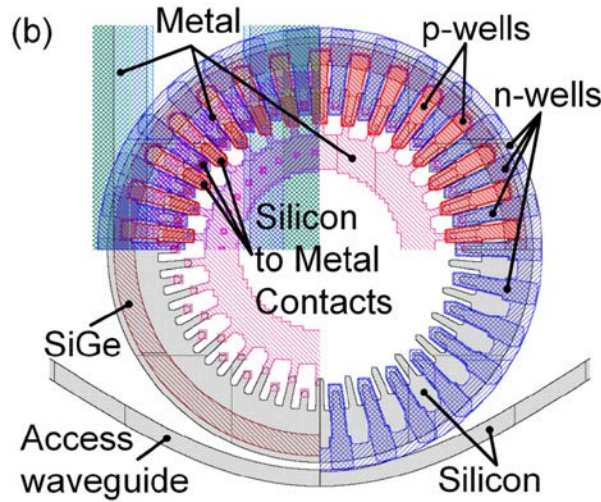


**Figure 3.2: Layout of the SiGe detector.** The interleaved PN junctions can be observed in red and blue. The SiGe film is highlighted in dark red [13].

When the device was designed, the reason for having a SiGe ring instead of pure silicon came from the increased free-carrier absorption of this material versus pure silicon. According to Drude's model, the free-carrier absorption is expressed by [17]:

$$\Delta\alpha = \left( \frac{q^3 \lambda^3}{4\pi^2 c^3 \epsilon_0 n} \right) \left[ \frac{\Delta N_e}{m_{ce}^{*2} \mu_e} + \frac{\Delta N_h}{m_{ch}^{*2} \mu_h} \right] \quad (3.1)$$

Where  $q$  is the electron charge,  $\lambda$  the operating wavelength,  $c$  the speed of light,  $\epsilon_0$  is the vacuum permittivity,  $n$  the refractive index,  $\Delta N_e$  and  $\Delta N_h$  the change in electrons and holes concentration, respectively,  $\mu_e$  and  $\mu_h$  the mobility of electrons and holes, and  $m_{ce}^*$  and  $m_{ch}^*$  are the conductivity effective masses of electrons and holes, respectively.

Since  $\text{Si}_{0.7}\text{Ge}_{0.3}$  has increased hole mobility with respect to pure Si, the absorption of free-carriers will be enhanced due to the SiGe pocket present in our device. Therefore, since more carriers will be absorbed, the amount of electron-hole pairs that will be created will be higher (Section 2.2.2) and then the amount of current also higher.

The devices were tested by and reported in February 2016 [13]. In Figure 3.3 the IV curve of the photodiode is shown. The device shows a dark current smaller than 20 pA. The device also shows a higher current at resonance than far from resonance. This is a normal



behavior in ring-resonator detectors. As explained in Section 2.2 when the light at the input is at the resonant wavelength of the ring, the light inside the ring and the one in the waveguide interfere constructively, having more light then circulating in the ring and therefore increased responsivity. When far from resonance, there is destructive interference between the ring and the waveguide, and then the current generated is smaller.

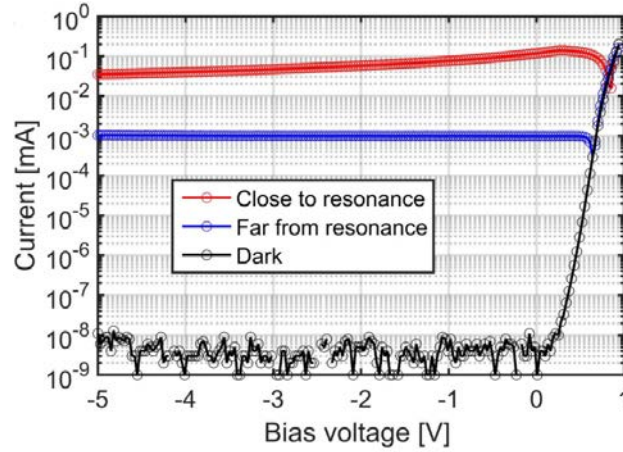


**Figure 3.3: IV characteristic of the detector.** The greatest current is achieved when close to resonance because of the in-phase interference of waveguide and ring [13].

Another important feature measured was the 3 dB bandwidth. Figure 3.3 shows the 3 dB bandwidth measured with both 0V bias and -4V bias. The reason for choosing reverse bias operation is because the energy barrier between P region and N region increases, the depletion width is higher and there is more chance for photoabsorption to happen there. This is the reason for having increased bandwidth with -4 V. The detector shows a 3 dB bandwidth of 5 GHz at -4V bias with 100  $\mu$ A average photocurrent.

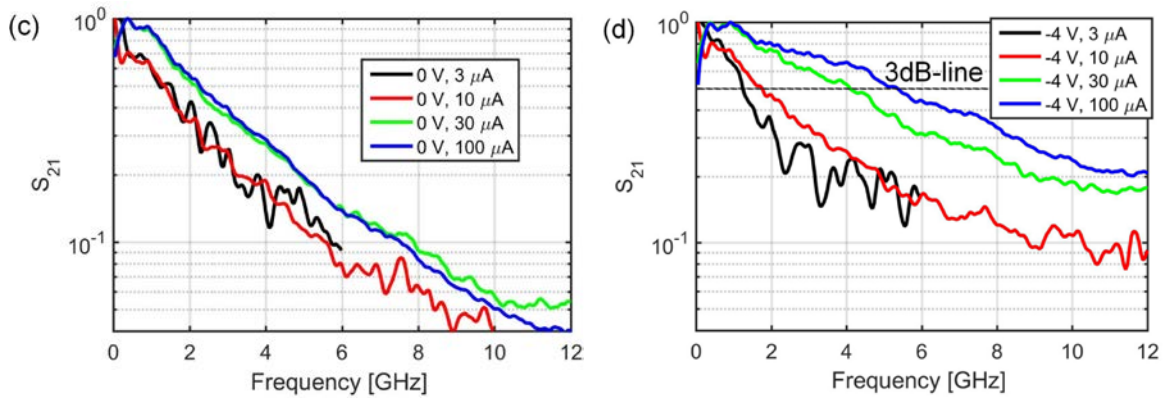


**Figure 3.4: Frequency response with different illumination conditions at (c) 0V bias and (d) 4V reverse bias [11].**

An important aspect of this device is that it shows a current-dependent bandwidth. It has been shown by posterior simulations that because of the weak doping, the photocurrent actively changes the depletion width by injecting carriers [19]. With an increase in the doping, this problem is solved and there is no bandwidth dependence with photocurrent.

### 3.1 Plasma-dispersion enhancement

As we have explained, when working as a detector, the key feature of this ring is the increased responsivity achieved due to the SiGe film etched in the PN junction. When working as a modulator, one of the key features in order to achieve great ER with low power consumption is the wavelength shift achieved when applying voltage. We will show in this section that SiGe enhances the plasma-dispersion effect and therefore we will achieve more wavelength shift with the same voltage than in a pure Silicon device.

As shown by [20], a SiGe device can increase the modulation efficiency based on plasma-dispersion effect. This enhancement in the modulating efficiency arises from the decreased effective conductivity mass of SiGe with respect to pure Si devices. In Section 6.2 there is a theoretical approximation of Soref's equations from Drude's model.

The expression that outputs Drude's model is [17]:

$$\Delta n = - \left( \frac{q^2 \lambda^2}{8\pi^2 c^3 \epsilon_0 n} \right) \left[ \frac{\Delta N_e}{m_{ce}^*} + \frac{\Delta N_h}{m_{ch}^*} \right] \quad (3.2)$$

It can be observed that all the variables are constant except for the refractive index  $n$  and the effective conductivity mass of both electrons and holes  $m_c^*$ . The change in refractive index due to the plasma-dispersion effect is inversely proportional to  $m_c^*$ . Therefore, the lighter the carriers are, the greater is  $\Delta n$ .

From [22], and [23], the effective conductivity mass of holes for pure Si is  $0.36m_0$ , whereas for  $\text{Si}_{0.7}\text{Ge}_{0.3}$  is  $0.14m_0$ , where  $m_0$  is the vacuum electron mass. This difference increments the effective refractive index change and therefore will enhance the modulation efficiency.

In Figure 3.5 reported by Kim *et al.* [20], we can observe a theoretical increase of the change in refractive index depending on the germanium fraction of  $\text{Si}_{1-x}\text{Ge}_x$ . With  $x=0.3$ , an approximate 2.5-fold increase is observed from using  $\text{Si}_{0.7}\text{Ge}_{0.3}$  with respect to using Si. Although the paper reports the results for injection-type pure SiGe modulator, this illustrates the benefit of putting a SiGe pocket in our design.

To the best of our knowledge, there has been only one SiGe – based optical modulator in silicon photonics [21]. However, this modulator was injection-based, whereas ours is depletion-based. Moreover, our work is the first-ever resonant modulator using SiGe as an active material.

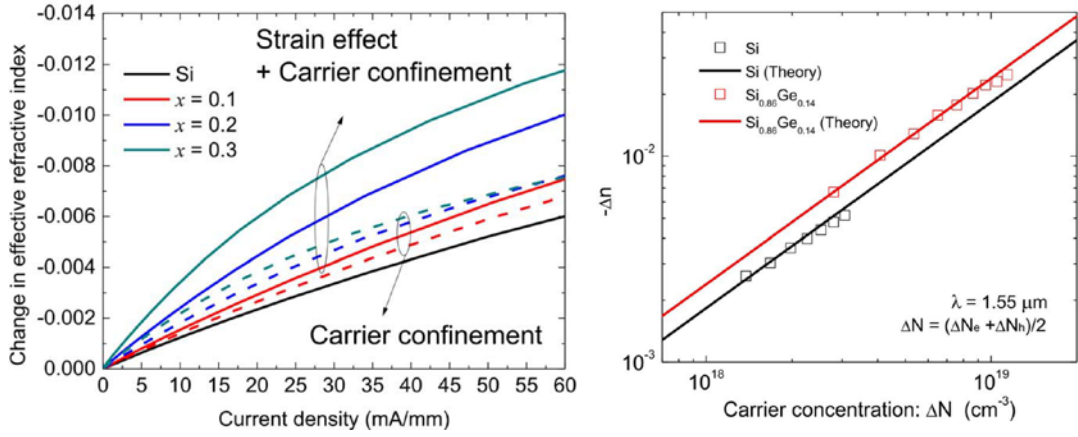


**Figure 3.5: Left: Theoretical refractive index change with change in the Ge fraction in  $\text{Si}_{1-x}\text{Ge}_x$  in an injection SiGe modulator. Right: Experimental demonstration with a  $\text{Si}_{0.86}\text{Ge}_{0.14}$  modulator [20].**

### 3.2 Working principle. Assumptions taken

The main assumption for the explanation of the working principle of our SiGe modulator is that the SiGe layer is lightly p doped. In that way, the depletion of the carriers happens in both the interleaved PN junction as well as between the N and the SiGe layer (p-), having something similar to a vertical junction as well. Some simulations in *Sentaurus* are being run in order to confirm this hypothesis.

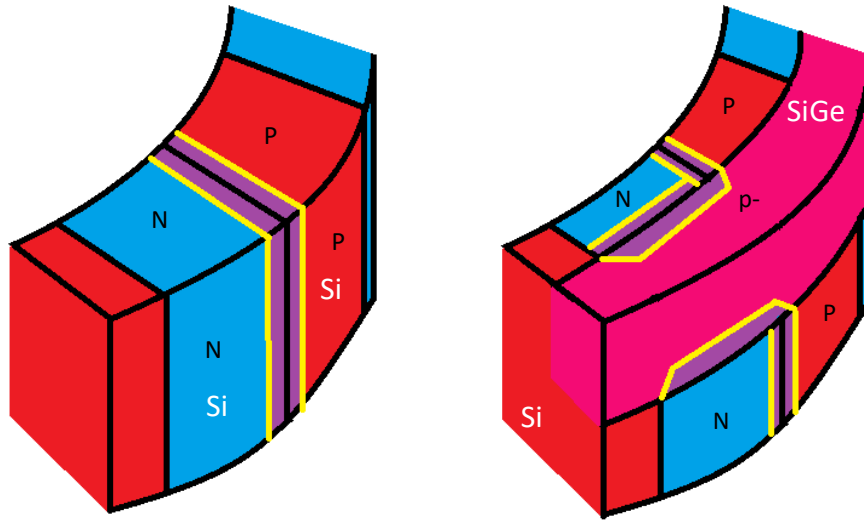


**Figure 3.6: Diagram of a section of a ring resonator, showing the depletion regions in purple.**

**Left: pure Si device, the depletion happens in the union between P and N. Right: SiGe ring resonator. The SiGe layer is assumed to be p-, having depletion between P and N and p- and N.**

In this way, since we have drift and diffusion happening in SiGe, there is a change in the carrier concentration of SiGe. In that way, as the effective mass of SiGe is smaller than in Si, more wavelength shift is achieved. If SiGe was intrinsic, all the theory explained about the enhanced plasma effect coming from the Drude model would not apply, since there would be no change in carrier concentration taking place in SiGe.

# 4 Experimental results

In this section we will explain the experimental results obtained by measuring the explained ring resonator as a modulator. We will cover the three main measurements done: DC measurements, bandwidth measurements and temporal domain measurements.

## 4.1 DC measurements

A diagram of the experimental setup is shown in Figure 4.1. It is the experimental setup for the DC measurements, but it is common for all types of experiments, since at the beginning of each experiment some DC measurements were needed (e.g. transmission curve measurement).

The light is generated by a broadband tunable laser, *SANTEC Full-band tunable laser TSL – 210F*. Then, in order to compensate possible polarization misalignments of the input light a polarization controller is put (*FIBER CONTROLLER INDUSTRIES FPC-2*).

The reason for having 90-10 couplers (*THORLABS 10202A 30-APC*) in the setup is to compensate for two imperfections: the first one is that the laser does not output a constant power among all the wavelength range; therefore, the power at the output of the laser is subtracted to the one received at the output of the ring. The optical power is read with an optical power meter (*HP81532A*). There is also a misalignment between the set and read wavelengths, therefore, a wavelength reader is put (*BRISTOL 621 Wavelength Meter*).

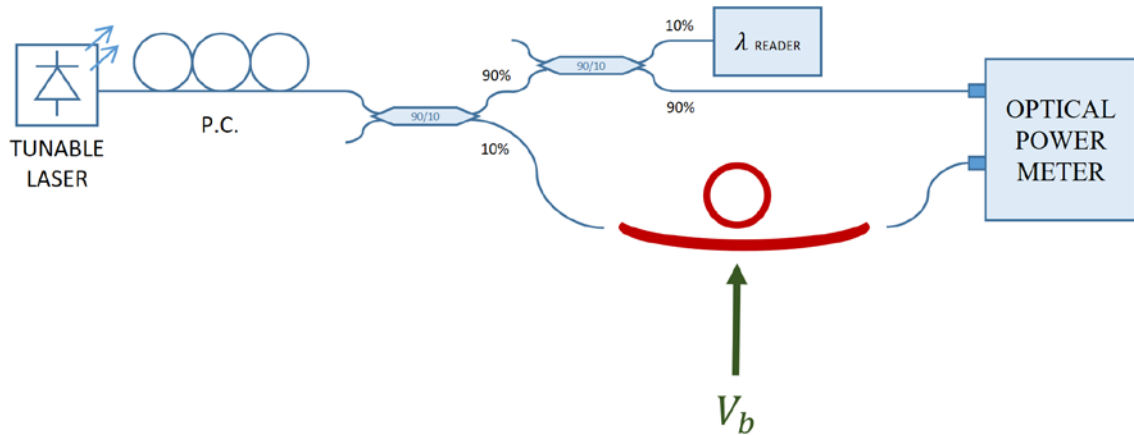


**Figure 4.1: Experimental setup for the DC measurements.** Blue: optical signal. Green: electrical signal. Red: SiGe modulator. PC: Polarization controller.

The light is coupled into and out of the modulators via lensed fibers (*OZ OPTICS TSMJ-3U-1550-9/125-0.25-7-5-26-2*). The particularity of the lensed fibers is that their tip ends in a cone-shaped way, therefore, the light is pointed better into the GC and then coupled better in

and out of the ring. Experimentally, each of the lensed fibers provides about 3 dB gain with respect to 90°-cut fibers.

The electrical signal is supplied through a 50  $\mu\text{m}$  GS probe (*CASCADE MICROTECH Infinity 167-A-GS-50*) landed on the electrical pads of the resonator. The GS probe has been used both for providing signal to the modulator and for sensing the photocurrent generated by the cavity.

In order to ease the process of coupling the light into the ring, a microscope with an infrared camera have been used. These elements do not play a key role in the final results, although they have been very useful in terms of speeding up the process of coupling light into the chip.

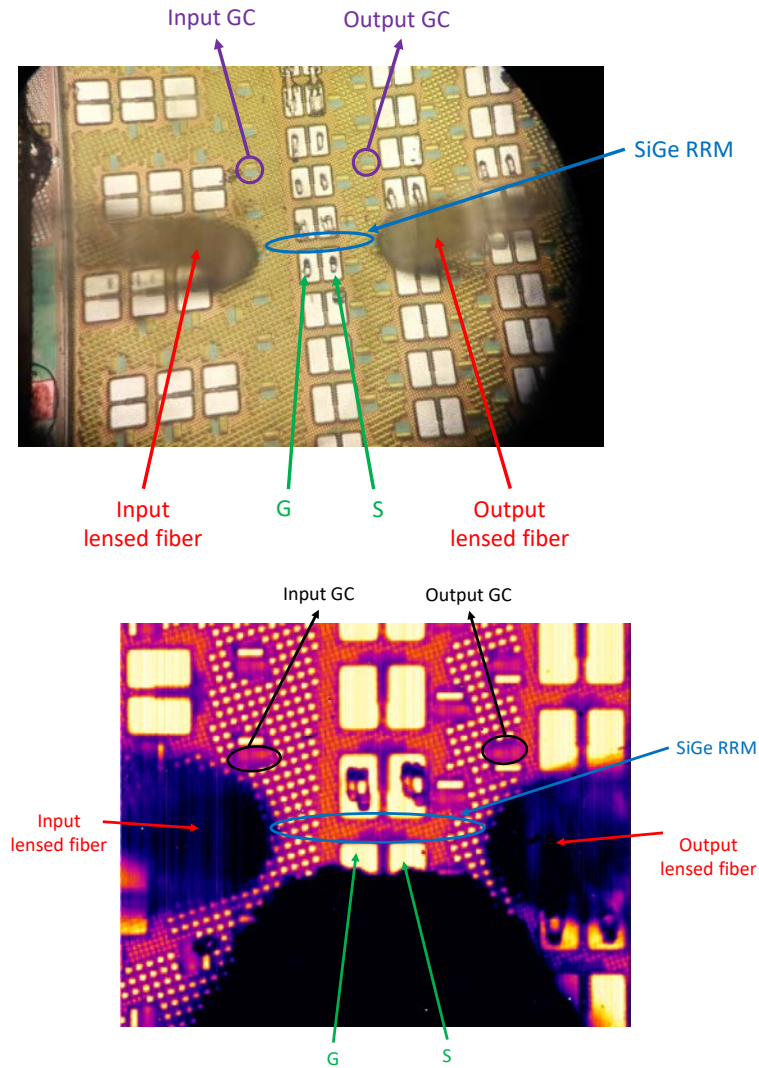


**Figure 4.2: Microscopic (top) and IR camera vision (bottom) of the setup.** The position of the fibers is initially optimized visually with the help of the IR camera. After that, polarization and further position optimization is done based on the received power.

All the devices have been tested, and the one that has shown best performance is the one at 260 nm distance between the ring and the waveguide (260 gap). This is the one that we will report.

#### 4.1.1 IV curve

One of the first things to do when characterizing a PN junction device is to measure its IV curve. We compare the IV curve of our modulator, the SiGe ring resonator modulator, with a pure-Si modulator device [11].

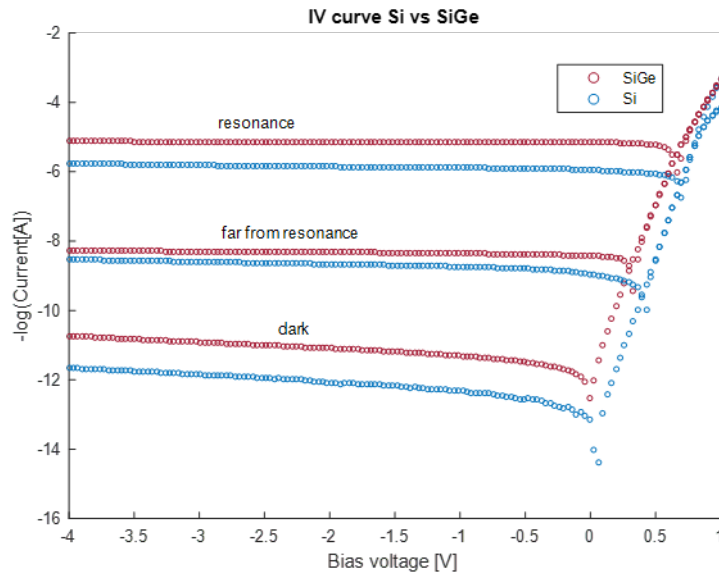


**Figure 4.3: IV curve comparison between Si modulator and SiGe modulator.** Both act as a photodetector when modulating.

As it can be observed, both devices act as photodetectors, creating electron-hole pairs when the light is going through the ring. As explained in section 3, the increased mobility of holes in SiGe makes the absorption higher than in pure Si, leading to higher photocurrent.

#### 4.1.2 Free spectral range (FSR)

The Free Spectral Range is defined as the distance in wavelength among resonances. The parameter depends mainly on the geometry of the cavity; the ring radius  $r$  defines the periodicity. This is an important parameter for defining Wavelength Division Multiplexing (WDM) channels in a complete system.

As we explained in Section 2.2.1.1, the transmission null is reached when there is a  $\pi$  phase difference between the wave transmitted through the waveguide and the one outputted by the ring. This destructive interference could happen always with a  $(2m + 1) \cdot \pi$  phase difference, being  $m$  an integer. This is the reason for having periodic resonances.

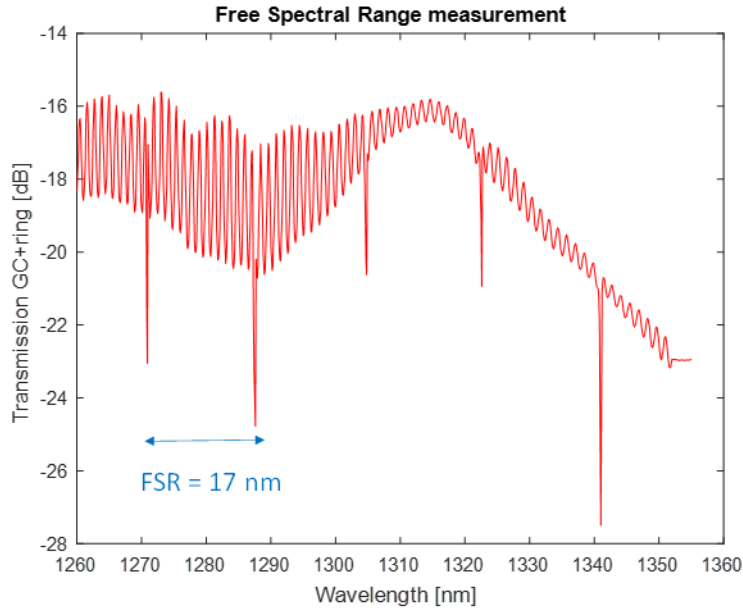


**Figure 4.4: Free spectral range measurement.**

The measured FSR is 17 nm. This is a number comparable to *Shainline et al.* [10] which was also tested to be 17 nm with a 5  $\mu\text{m}$  radius ring, too. The Fabry-Perot oscillation observed off-resonance is a non-ideal effect of the grating couplers.

#### 4.1.3 Resonance parameters

When talking about the transmission curve, there are three main aspects to take into account for evaluating the performance of the device: the  $Q$  factor, the extinction of the curve at resonance and the Insertion Loss of the ring.

The higher the  $Q$ , the narrower will be the Lorentzian. Therefore, the less power consumption (voltage) will be needed in order to achieve the same ratio between the two power levels (ER), as less shift will be needed.

The extinction of the curve is also important. The extinction of the resonance is defined as the amount of attenuation that the optical power suffers at resonance. Therefore, an ideal transmission curve will have an extinction equal to  $\infty$ . A device with a low resonance extinction directly affects the ER of the temporal signal, having then a closed eye diagram.

A transmission curve of our modulator is depicted in Figure 4.5. The extinction (relation between non-resonance and resonance) is around 18.5 dB.

The loaded  $Q$  is defined as:

$$Q = \frac{\lambda}{\delta_{FWHM}} \quad (4.1)$$



Where  $\delta_{FWHM}$  is the Full-Width-Half-Maximum (FWHM) transmission of the device, defined as the point with 3 dB transmission with respect to the non-resonance point. In our case  $\delta_{FWHM} \approx 0.28 \text{ nm}$ , leading to a loaded  $Q$  of 4500.

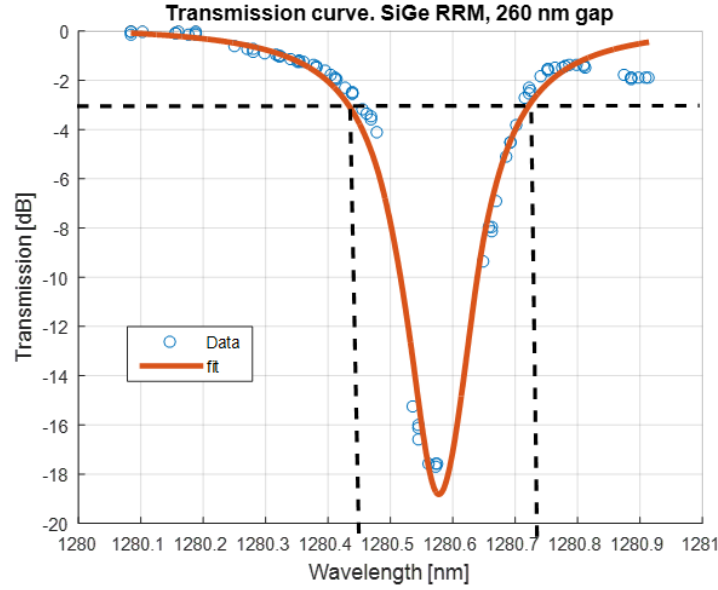


**Figure 4.5: Transmission curve with 4V reverse bias.**

The Insertion Loss (IL) is defined as the additional loss inserted by the ring. The IL introduced by the grating couplers (GC) is not taken into account, since we are only talking about the modulator.

We have not had the possibility of measuring the IL of the gratings alone, since we do not have the appropriate test structure to measure them. However, in order to quantify the extra loss of the ring alone, we have made measurements with two rings: the first one with the smallest gap (170 nm) and the second one with the biggest gap (290 nm). The difference in the transmission curve out of resonance gives us the additional IL introduced by the ring.

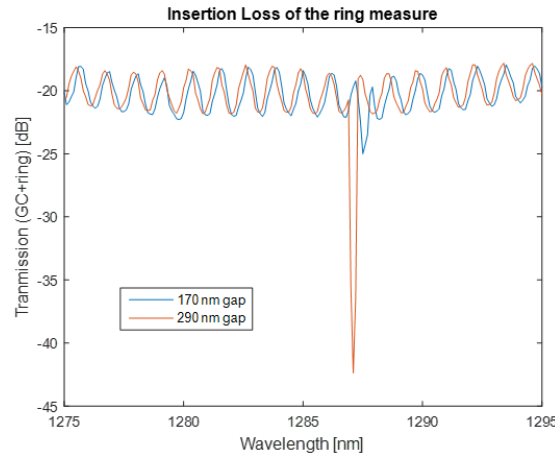


**Figure 4.6: Transmission curve at -4V for the devices at maximum and minimum gap. The IL added by the ring is negligible.**



It can be seen that the power off-resonance is the same in both modulators, having a small shift in wavelength, that could be due to non-ideal heating effects or coupling difference. Therefore, we will assume that all the IL in the device comes all from the GC, and that the ring does not introduce any additional loss.

#### 4.1.4 Wavelength shift

The most important measurement done is the wavelength shift when changing the bias voltage. The device shows an increment in 33% in the wavelength shift with modulation versus a pure silicon device.

As explained in Section 3.1, the reduced conduction effective mass of the holes in SiGe makes an increment in the refractive index change, leading to an increment in the wavelength shift with voltage. Figure 4.7 depicts the resonance curve applying 1 and 4V reverse bias.

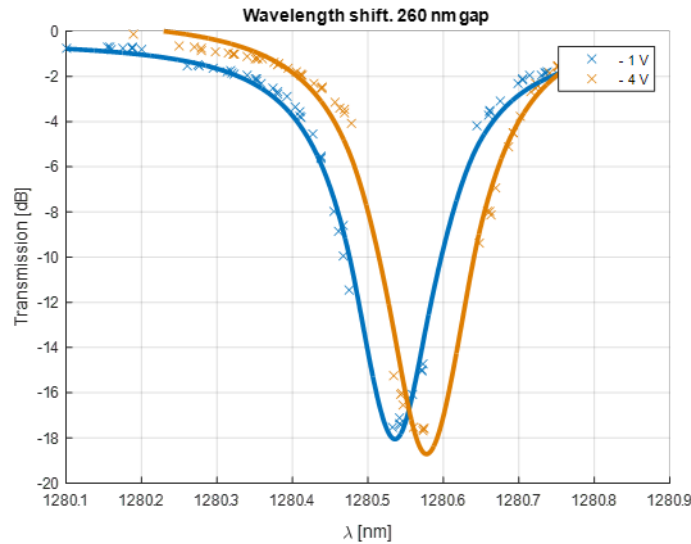


**Figure 4.7: Transmission curves at -1V and -4V.**

Figure 4.8 depicts the wavelength shift comparison between our SiGe ring modulator and *Alloatti et al.* Si modulator [11]. We have measured 5 times the wavelength shift for each bias voltage, comparing to 0V, and we have plot the mean and the standard deviation for both SiGe and Si devices.

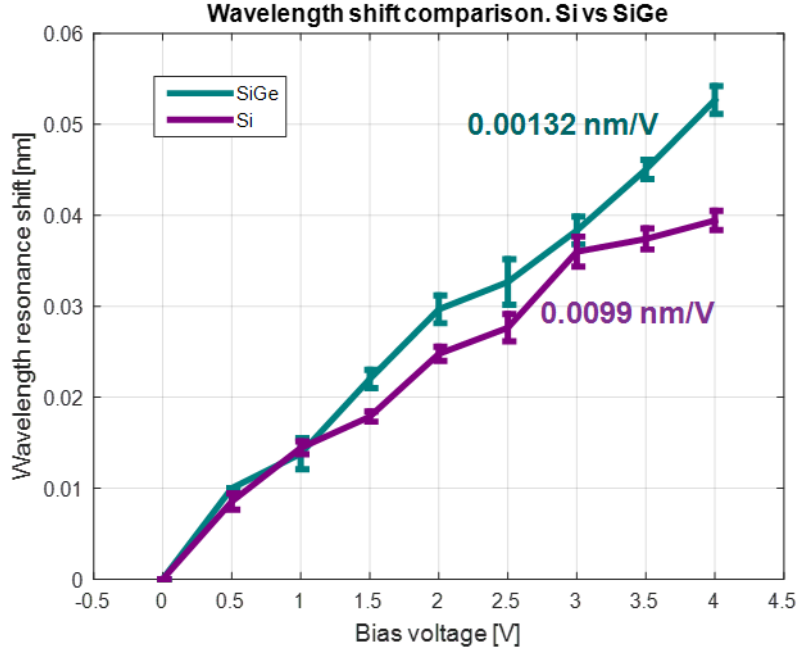


**Figure 4.8: Wavelength shift comparison between Si and SiGe modulators.** 5 measurements for each bias point have been taken. Mean +/- std deviation is plotted.

Due to the reduced effective mass of the holes, the modulator increases the plasma-dispersion effect, resulting in a 33% increment in the wavelength shift.

## 4.2 Frequency measurements

The experimental setup for the frequency measurement is depicted in Figure 4.9. The Vector Network Analyzer (VNA) generates a small amplitude signal (considered as small-signal modulation) in a frequency range defined by the user. The outputted signal and the signal inputted through another channel are compared. Based on that comparison, it calculates the  $S_{21}$  parameter.

The electrical RF signal is generated by the VNA (*HP 722D*). The DC signal is generated by a sourcemeter (*KeySight B2902A*) also used to sense the generated photocurrent. Both signals are mixed with a bias-T (*SHF BT 65B*).

In order to have enough signal at the input of the VNA, amplification of the signal is needed. For doing so, a Semiconductor Optical Amplifier (SOA) (*THORLABS BOA 1130S*) is put after the modulation of the signal. To avoid the Amplified Spontaneous Emission (ASE) noise of the amplifier, we put an optical filter (*KOSHIN KOGAKU FC-1300B-1-1*). Optical isolators (*THORLABS P/N IO-H-1310-APC*) are also put after and before the amplifier to avoid reflections going to the ring. The optical amplified signal is then converted to the electrical domain with a commercial photodiode (*DISCOVERY SEMICONDUCTORS DSC30-3-2010*).

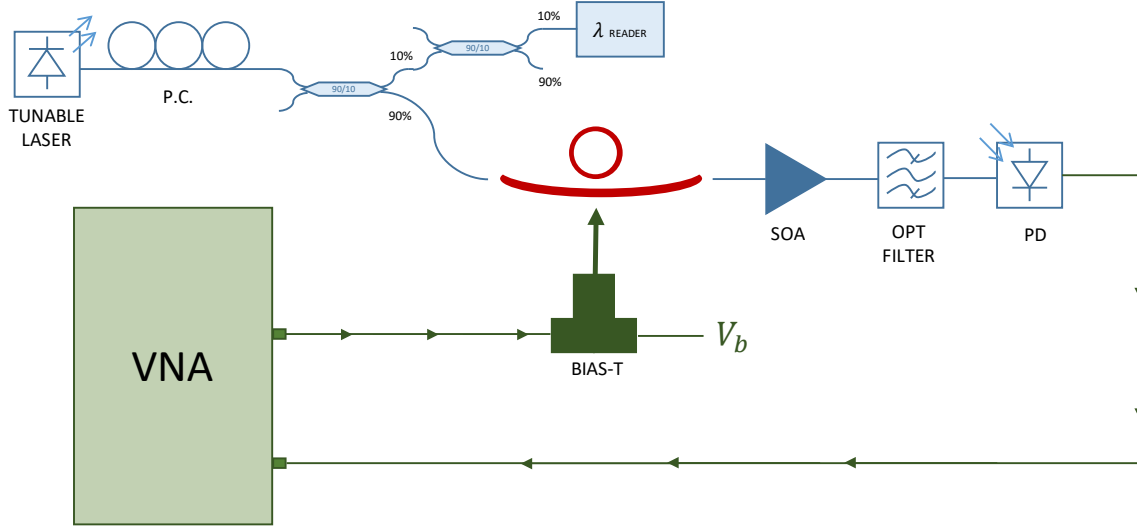


**Figure 4.9: Experimental setup for the bandwidth measurement.** Blue: optical signal. Green: electrical signal. Red: SiGe modulator. SOA: Semiconductor Optical Amplifier. PD: photodiode.

Several measurements have been taken, varying the bias offset. The bandwidth of the device has been proven to be current dependent, as reported in [13] when testing the device as a photodiode. Besides, the bandwidth of the device is also dependent on the wavelength. This dependence strongly depends on the slope of the transmission curve, since it is a small-signal modulation.

Figure 4.10 shows three different measurements at three different wavelengths. The resonance wavelength is 1280.57 nm, that is the wavelength that shows less bandwidth. The reason for having this small bandwidth is because in resonance, the transmission curve has slope close to zero. Thus, change in the electrical signal translates into a small change in the optical domain. As the measurement can be considered as small-signal modulation, by taking the derivative we can observe (Figure 4.10 bottom right) that the slope is close to zero at the resonance point.

The other two positions represent points close to the maximum slope point, in order to have increased bandwidth. The difference in terms of photocurrent comes from different coupling of the fibers. We have changed the position in every measurement, since misalignments happen often. In this case we show the current dependency of the bandwidth, since both wavelengths have the same slope.

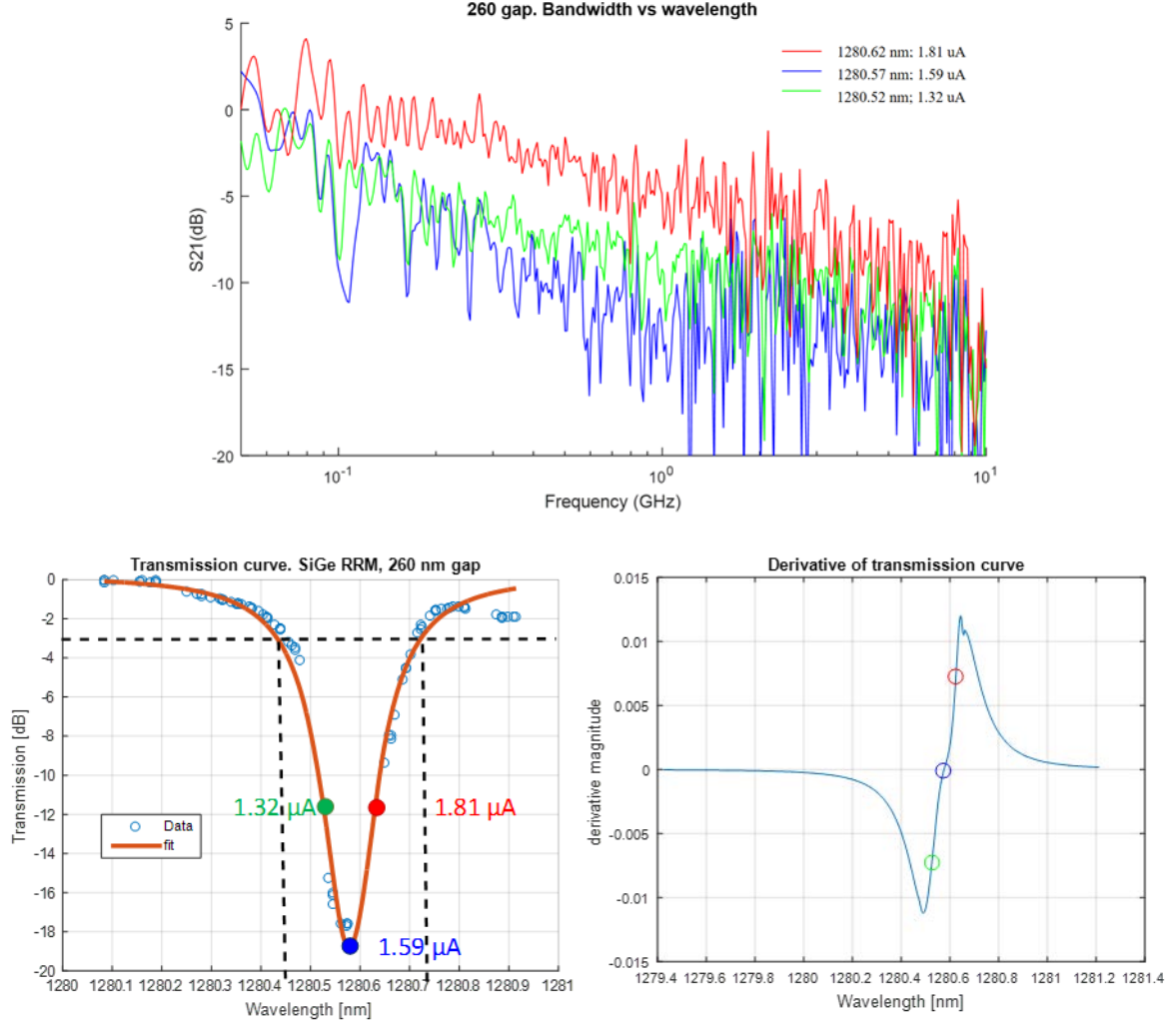


**Figure 4.10: Top:  $S_{21}$  measurement with -4V bias voltage, at 3 different wavelengths.**

**Bottom left: measured wavelengths superimposed in the transmission curve.**

**Bottom right: measured wavelengths superimposed in the derivative of the transmission curve.**

The 3 dB bandwidth of the device, after fitting the data, is 360 MHz (Figure 4.11). Nevertheless, the decay over frequency is small, having the 10 dB bandwidth at 5.5 GHz.

The bandwidth is so small due to the inherent RC limitation of this particular design of the interleaved junctions, due to parasitic capacitances between silicon and the metal contacts. There is a proposed solution, the called “T-junction” that overcomes this problem. It concentrates the capacitance in the optical region and minimizes the parasitic capacitance. There are already designed devices working with T-junctions with simulations showing a greater bandwidth than conventional interleaved PN junctions [24].

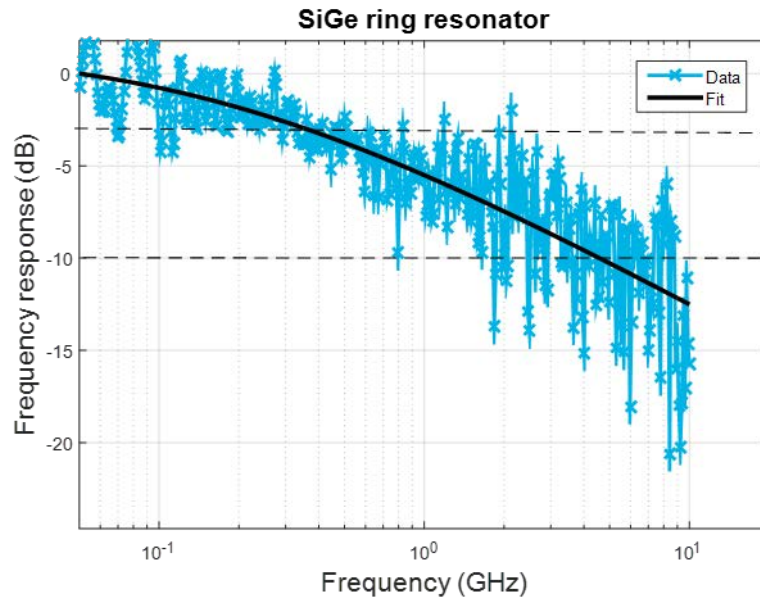


**Figure 4.11: Fitted 3 dB bandwidth of the SiGe modulator.** The 3 dB point is at 360 MHz, whereas the 10 dB decay is at 5.5 GHz.

### 4.3 Eye diagram

In order to know the performance of the modulator under high-speed conditions, the eye diagram has been measured. The experimental setup for doing so is depicted in Figure 4.12. The modulation signal has been chosen to be a Pseudo-Random Binary Sequence (PRBS) length  $2^{23}-1$  with a high-speed pattern generator (*Agilent 70843B*). The eye is displayed in the oscilloscope (*HP 83480A*) receiving the signal on the optical channel input (*HP 83485A*).

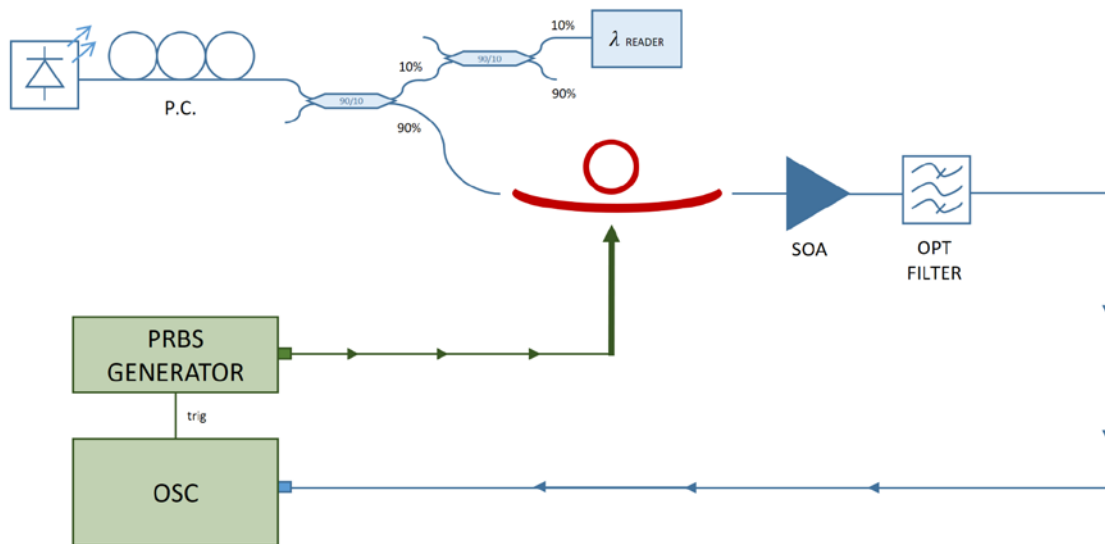


**Figure 4.12: Experimental setup for the eye diagram measurement.** Blue: optical signal. Green: electrical signal. Red: SiGe modulator. OSC: Oscilloscope.

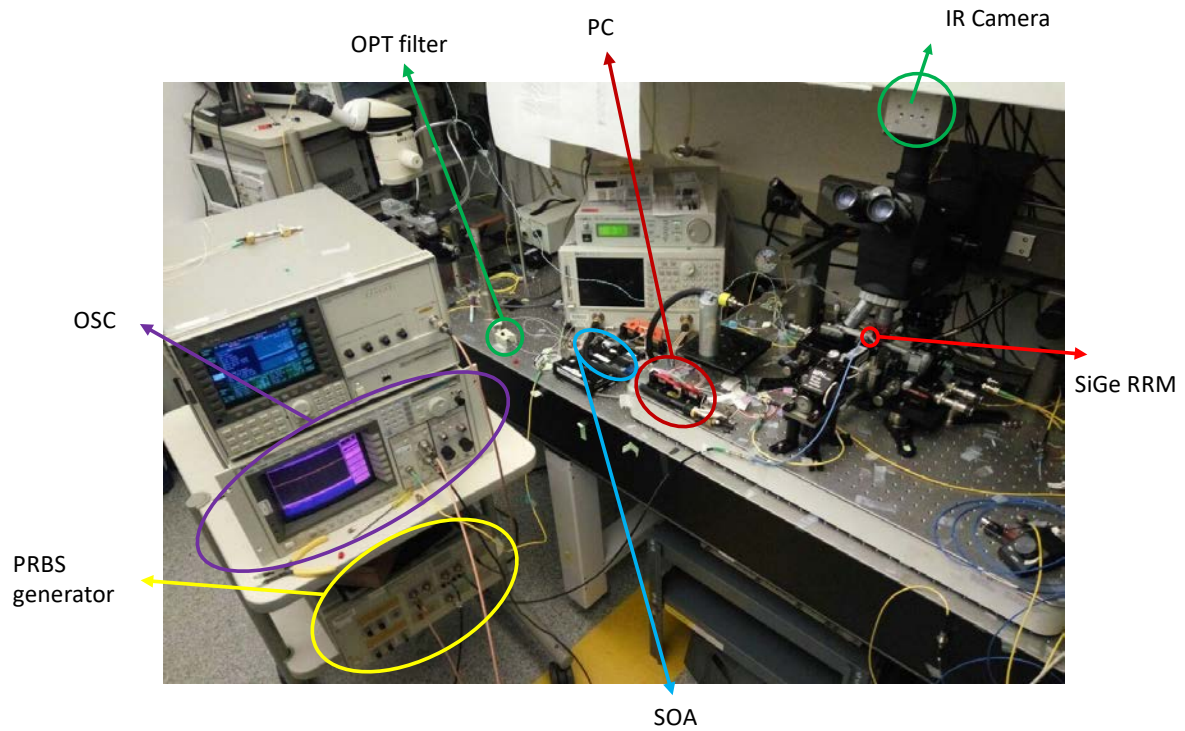


**Figure 4.13: Picture of the experimental setup.**

The eye diagram shown in Figure 4.14 is recorded at 2.5 Gbps, 3 V<sub>pp</sub> amplitude at the terminals of the ring. It shows a great ER of 9.6 dB, coming from the increased modulating efficiency of the device thanks to the SiGe layer.

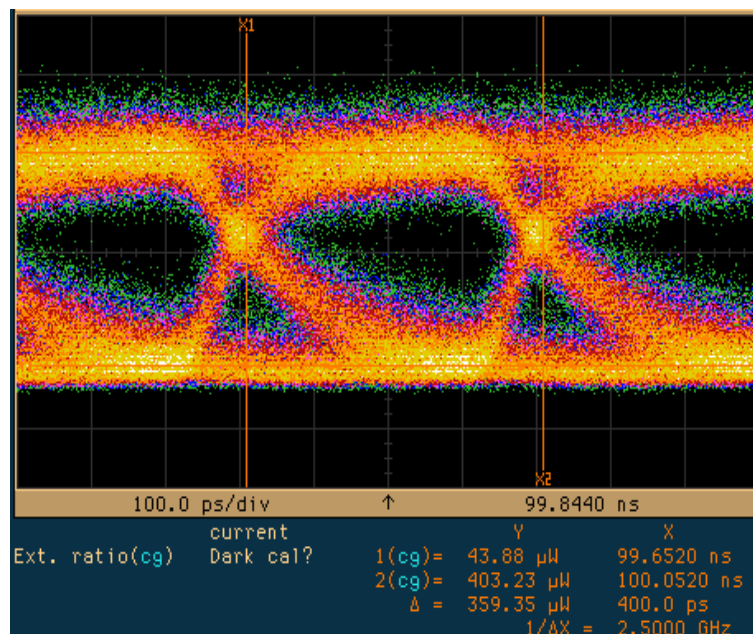


**Figure 4.14: Eye diagram at 2.5 Gbps, with 3V<sub>pp</sub> amplitude at the terminals of the device.**

The IL of the modulation is estimated to be around 3.48 dB. This calculation has been done taking into account the power off-resonance, 900  $\mu$ W. The ratio between the optical “1” and the power out of resonance is the insertion loss of modulation.

### 4.3.1 Asymmetry of the eye diagram

We can observe that the eye diagram is not symmetric. This comes from the signal inputted to the modulator. In the PRBS generator, we have configured a 1.5 V signal, going from 0V to -1.5 V. The device is approximated as an open circuit, so we need to approximate the driving voltage as doubling at the open terminals. The DC value remains constant, so we have an effective driving voltage at the PN junctions of 3 V<sub>pp</sub>, swinging from 0.75 V to -2.25V.

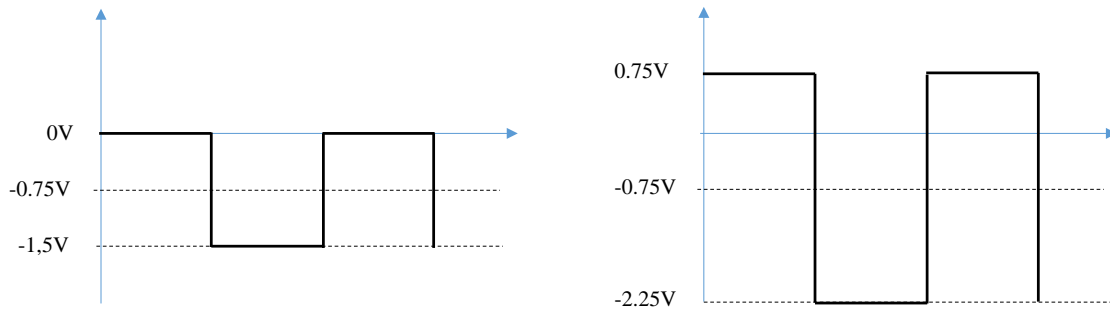


**Figure 4.15: Left: Electrical signal at the output of the PRBS generator.**

**Right: Effective signal at the terminals of the device.** Due to infinite impedance approximation, the voltage effectively doubles.

This means that one of the transitions will be dominated by forward bias, whereas the other transition is reverse-biased dominated. As explained in Section 2.1.1, a forward biased junction is dominated by diffusion current, which is slower than the drift current (reverse-biased junction). This corresponds to the transition from the optical “1” to “0”, and is the reason for having a slower response than the other.



# 5 Conclusion

---

A migration to photonic interconnects in microprocessor environments is needed in order to overcome the bottleneck of the electrical wiring networks in terms of speed and power consumption.

In this thesis we have studied a SiGe ring resonator modulator that could act in the future as a main component fulfilling next-generation supercomputer interconnect requirements. The modulator has been characterized both theoretically and experimentally.

We have completed the first ever demonstration of a SiGe resonator depletion modulator. The device was manufactured under zero-change CMOS technology (Global Foundaries/IBM 45 nm SOI process), enabling low-cost and easy integration with state-of-the-art electronics.

The device shows 33% increased modulating efficiency compared to a pure silicon device. The reduced conductivity hole effective mass present in SiGe with respect to Si makes this change possible.

The measured FSR is 17 nm, coming from the 5  $\mu\text{m}$  radius of the ring. The loaded Q of the device is around 4500, with an extinction at resonance of 18.5 dB. The extra IL added by the ring is approximated to be 0 dB.

The measured 3 dB bandwidth is 360 MHz. An opened eye diagram at 2.5 Gbps has been demonstrated, with  $3V_{pp}$  driving voltage. The enhanced wavelength shift with respect to Si devices makes the ER to be 9.6 dB. The IL of modulation is around 3.5 dB.

The device shows the biggest reported wavelength shift up to the date for zero-change CMOS devices. This demonstration opens a new era of design of silicon photonic modulators using silicon-germanium as an active material.



## 5.1 Future work

The work of designing zero-change CMOS devices has been present in the group for more than 10 years. Therefore, plenty of possibilities for future work related to this thesis are open.

First of all, we need to confirm that the assumption of having diffusion going on in SiGe is true. For doing so, an upper bound for the SiGe doping has been calculated. We assumed that the Quantum Efficiency (QE) was limited by the absorption, and plugging that to the Drude model Eq. (3.1), it gave us an upper bound of the acceptor concentration  $N_A$ . With this number, simulations are being run in *Sentaurus*, in order to confirm that there is depletion region between the interleaved P and N and the p- and N as well.

The next step would be to explore further geometries in order to exploit the benefit of having SiGe as an active material in modulation. Also, to design and manufacture devices based on the T-junction, overcoming the problem of the parasitic capacitance, that RC-limits the bandwidth.

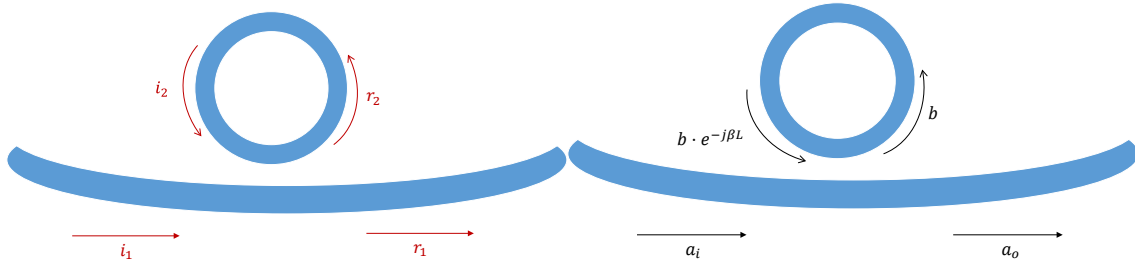
A characterization of these devices for long-haul applications is also needed. There could be a potential application for these devices in telecommunication applications, enabling low-cost modulators and detectors, as well as filters. For doing so, for example for modulators a key parameter is the chirp of modulation. If the chirp is high, when transmitting the data through a dispersive material (optical fiber) leads to nulls in transmission that can kill your signal.

Finally, we have demonstrated a modulator that was already tested as a detector. We could think about potential applications for this device, that depending on the input (electrical or optical) it becomes a modulator or a photodiode. The most straightforward solution would be to reduce the number of optical lines for microchip applications from two to just one.

# 6 Appendix

## 6.1 Transmission derivation in an optical ring resonator

For understanding the behavior of the ring we will derive the expression for the transmission curve. For doing so, we can understand the ring as a two-port network in which we can represent the power waves in a matricial manner, where  $\kappa$  is the coupling coefficient between waveguide and ring and  $t$  is the transmittance of the waveguide.



$$\begin{bmatrix} r_1 \\ r_2 \end{bmatrix} = \begin{bmatrix} t & -j\kappa \\ -j\kappa & t \end{bmatrix} \cdot \begin{bmatrix} i_1 \\ i_2 \end{bmatrix} \quad (6.1)$$

Leading then a pair of equations:

$$\begin{cases} a_o = ta_i - j\kappa \cdot b \cdot e^{-j\beta L} \\ b = t \cdot b \cdot e^{-j\beta L} - j\kappa a_i \end{cases} \quad (6.2)$$

$$b = -\frac{j\kappa a_i}{1 - t \cdot e^{-j\beta L}} \quad (6.3)$$

We then substitute the expression for  $b$  in order to calculate  $a_o/a_i$ :

$$\frac{a_o}{a_i} = t + \frac{(-j\kappa)^2}{1 - t \cdot e^{-j\beta L}} e^{-j\beta L} = \dots = \frac{t - (t^2 + \kappa^2)e^{-j\beta L}}{1 - te^{-j\beta L}} \quad (6.4)$$

Where, as we already know,  $\kappa$  is the coupling coefficient and  $t$  represents the transmittance. If the modulator is lossless (i.e. there are no heating losses, etc)

$$|\kappa|^2 + |t|^2 = 1 \quad (6.5)$$

Thus,

$$\frac{a_o}{a_i} = \frac{t - e^{-j\beta L}}{1 - t \cdot e^{-j\beta L}} \quad (6.6)$$

We know that the propagation constant  $\beta$  has a real and an imaginary part:

$$\beta = k_o n + j \frac{\alpha}{2} \quad (6.7)$$

Where  $\alpha$  is the absorption coefficient,  $k_o = \frac{2\pi}{\lambda}$  and  $n$  is the refractive index.

The condition for being at resonance is that the phase of the wave should be proportional to  $2\pi$ . This means that the real part of the propagation constant should be  $2\pi m$ . When close to resonance, the condition becomes

$$\beta_{close_{res}} l = (k_o \beta_{res} + k_o \Delta\beta) l = 2\pi m + \Delta\beta l \quad (6.8)$$

Therefore, we can re-write the transmission as:

$$\frac{a_o}{a_i} = \frac{t - e^{-j\beta_{close_{res}} l}}{1 - t \cdot e^{-j\Delta\beta_{close_{res}} l}} = \frac{t - e^{-j(\Delta\beta + j\frac{\alpha}{2})l}}{1 - t \cdot e^{-j(\Delta\beta + j\frac{\alpha}{2})l}} \quad (6.9)$$

We know by Taylor expansion that, when  $x \rightarrow 0$ ,  $e^{-x} \approx 1 - x$ . Thus, we can rewrite the expression as:

$$\frac{a_o}{a_i} = \frac{t - \left(1 + j\Delta\beta l - \frac{\alpha}{2}l\right)}{1 - t \left(1 + j\Delta\beta l - \frac{\alpha}{2}l\right)} \quad (6.10)$$

It can also be shown that:

$$\frac{\Delta\beta}{\Delta\omega} = \frac{1}{v_g} = \frac{1}{\frac{c_o}{n}} = \frac{n}{c} \quad (6.11)$$

Where  $\Delta\omega$  is the displacement in angular frequency from the resonance,  $v_g$  is the group velocity,  $c_o$  is the speed of light and  $n$  is the refractive index. Making use of this expression:

$$\frac{a_o}{a_i} = \frac{(t - 1) + \frac{\alpha}{2}l - j\frac{\Delta\omega}{c}nl}{(1 - t) + t\frac{\alpha}{2}l - jt\frac{\Delta\omega}{c}nl} \quad (6.12)$$

The quality factor ( $Q$ ) can be defined as the ratio between the stored energy and the dissipated energy in a complete cycle of a signal. In a ring resonator modulator, we can define 2 types of  $Q$ :

The coupling  $Q$ ,  $Q_c$ , determines the amount of energy that is coupled inside the ring. A lower  $Q_c$  means that more light goes inside the ring. On the other hand, the intrinsic  $Q$ ,  $Q_i$

determines the amount of energy lost by the ring in each cycle. A low  $Q_i$  means that less light is lost.

The expressions for both  $Q$  are:

$$Q_c = \frac{2\pi n l}{\lambda \kappa^2} \quad (6.13)$$

$$Q_i = \frac{2\pi n}{\lambda \alpha} \quad (6.14)$$

If we continue developing (6.12) multiplying and dividing by  $\frac{\lambda}{2\pi n l}$ :

$$\frac{a_o}{a_i} = \frac{(t-1) \frac{\lambda}{2\pi n l} + \frac{\alpha}{2} \frac{\lambda}{2\pi n} - j \frac{\Delta\omega}{c} \frac{\lambda}{2\pi}}{(1-t) \frac{\lambda}{2\pi n l} + t \frac{\alpha}{2} \frac{\lambda}{2\pi n} - j t \frac{\Delta\omega}{c} \frac{\lambda}{2\pi}} \quad (6.15)$$

We know that  $\omega = 2\pi f = 2\pi \frac{c}{\lambda}$ . If we consider the approximation  $t \approx 1$  and we plug it into (6.5), then  $|\kappa|^2 \ll 1$  and we do Taylor expansion:

$$(1-t) \approx \frac{\kappa^2}{2} \quad (6.16)$$

Taking into account this, we can continue the derivation:

$$\frac{a_o}{a_i} = \frac{-\frac{1}{2} \frac{\lambda \kappa^2}{2\pi n l} + \frac{\alpha}{2} \frac{\lambda}{2\pi n} - j \frac{\Delta\omega}{\omega}}{\frac{1}{2} \frac{\lambda \kappa^2}{2\pi n l} + \frac{\alpha}{2} \frac{\lambda}{2\pi n} - j \frac{\Delta\omega}{\omega}} \quad (6.17)$$

Knowing the expressions for  $Q_c$  and  $Q_i$ , we get to the final expression:

$$\frac{a_o}{a_i} = \frac{\frac{1}{2} \left( \frac{1}{Q_i} - \frac{1}{Q_c} \right) - j \frac{\Delta\omega}{\omega}}{\frac{1}{2} \left( \frac{1}{Q_i} + \frac{1}{Q_c} \right) - j \frac{\Delta\omega}{\omega}} \quad (6.18)$$

## 6.2 Theoretical derivation of Soref's Equations

Taking a look into Drude's model, the refractive index expression is:

$$n = \sqrt{1 - \frac{\omega_p^2}{\omega^2 + \gamma^2}} \quad (6.19)$$

Where  $n$  is the refractive index,  $\gamma$  is the damping force of the electron with its nucleus and  $\omega$  is its angular frequency. Coming from the microscopic Lorentz oscillator model, we know that  $\omega_p^2 = \frac{Nq^2}{\epsilon_0 m^*}$ . Therefore, we can rewrite the above expression as:

$$n = \sqrt{1 - N \cdot \frac{\frac{q^2}{\epsilon_0 m^*}}{\omega^2 + \gamma^2}} \quad (6.20)$$

Where  $q$  is the electron charge,  $\epsilon_0$  is the vacuum permittivity and  $m_c^*$  is the conductivity effective mass of the carrier. The angular frequency can be rewritten as  $\omega = \frac{2\pi c}{\lambda}$ , and the damping is inversely proportional to the lifetime. Moreover, mobility of the carriers is related to the lifetime  $\tau$ :

$$\gamma = \frac{1}{\tau}; \mu = \frac{q\tau}{m} \rightarrow \gamma = \frac{q}{m^* \mu} \quad (6.21)$$

Therefore, we can rewrite Eq. (6.20) as:

$$n = \sqrt{1 - N \cdot \frac{\frac{q^2}{\epsilon_0 m}}{\left(\frac{2\pi c}{\lambda}\right)^2 + \left(\frac{q}{m\mu}\right)^2}} \quad (6.22)$$

We will take, for an easy derivation,

$$n = \sqrt{1 - N \cdot C} \quad (6.23)$$

Where:

$$C = \frac{\frac{q^2}{\epsilon_0 m}}{\left(\frac{2\pi c}{\lambda}\right)^2 + \left(\frac{q}{m\mu}\right)^2} \quad (6.24)$$

To know the change in the refractive index  $\Delta n$  when changing the density of carriers  $\Delta N$ , we take the derivative of  $n$  with respect to  $N$  (Eq. (6.23)):

$$\Delta n = \frac{1}{2} \frac{-C}{\sqrt{1-CN}} \Delta N \quad (6.25)$$

Approximating  $CN \ll 1$ :

$$\Delta n = -\frac{1}{2} C \Delta N \quad (6.26)$$

$$\Delta n = -\frac{1}{2} \frac{\frac{q^2}{\epsilon_o m^*}}{\left(\frac{2\pi c}{\lambda}\right)^2 + \left(\frac{q}{m^* \mu}\right)^2} \Delta N \quad (6.27)$$

We can observe in the equation that the change in refractive index is inversely proportional to the carriers effective mass,  $m^*$ .

The equation also shows us that without the effective mass, all the other variables are constant among Si and SiGe, but the mobility of the carriers, that is increased in SiGe, as we explained before. However, since the effect is not noticeable here,  $\left(\frac{q}{m^* \mu}\right)^2 \ll \left(\frac{2\pi c}{\lambda}\right)^2$ , the effect of increased mobility in the change of refractive index is negligible.

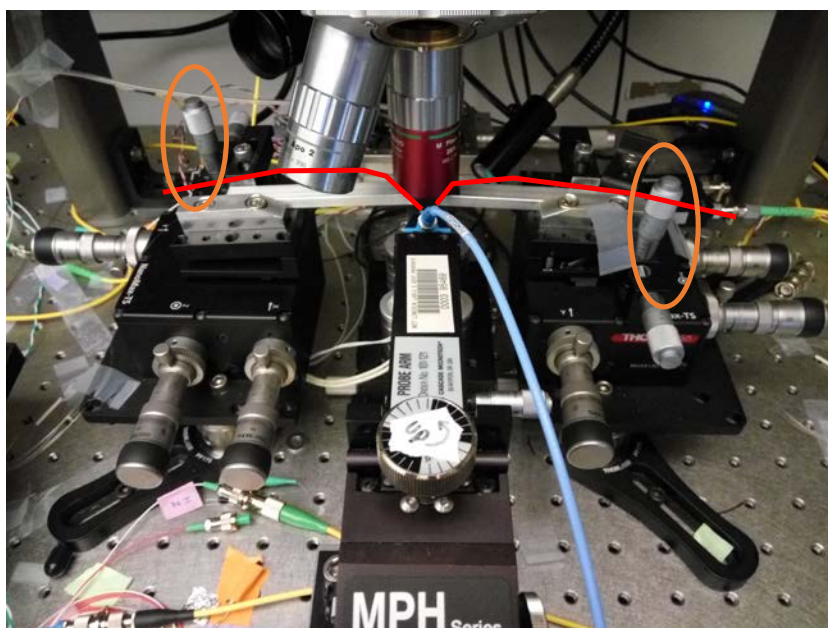
Therefore,

$$\Delta n = -\frac{1}{2} \frac{q^2 \lambda^2}{\epsilon_o 4\pi^2 c^2 n} \cdot \frac{1}{m^*} \cdot \Delta N \quad (6.28)$$

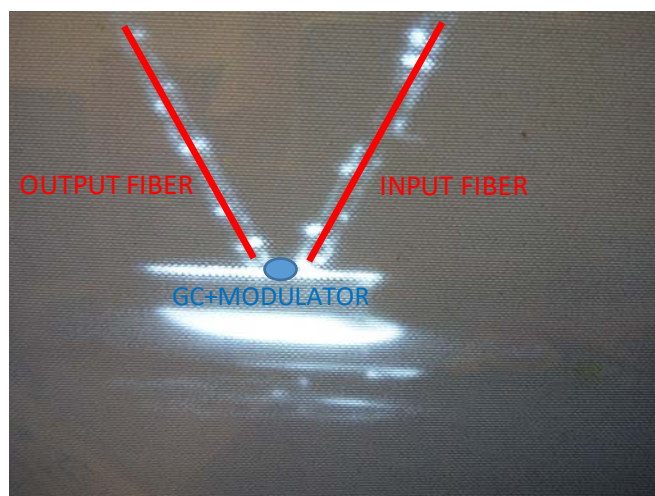
### 6.3 Optimization of the light incident angle

The incident angle of the light going into a grating coupler is a key point to take into account in order to maximize the signal. Depending on the incident angle, there is an optimum wavelength of operation, where the grating coupler power that goes into the waveguide is maximized.

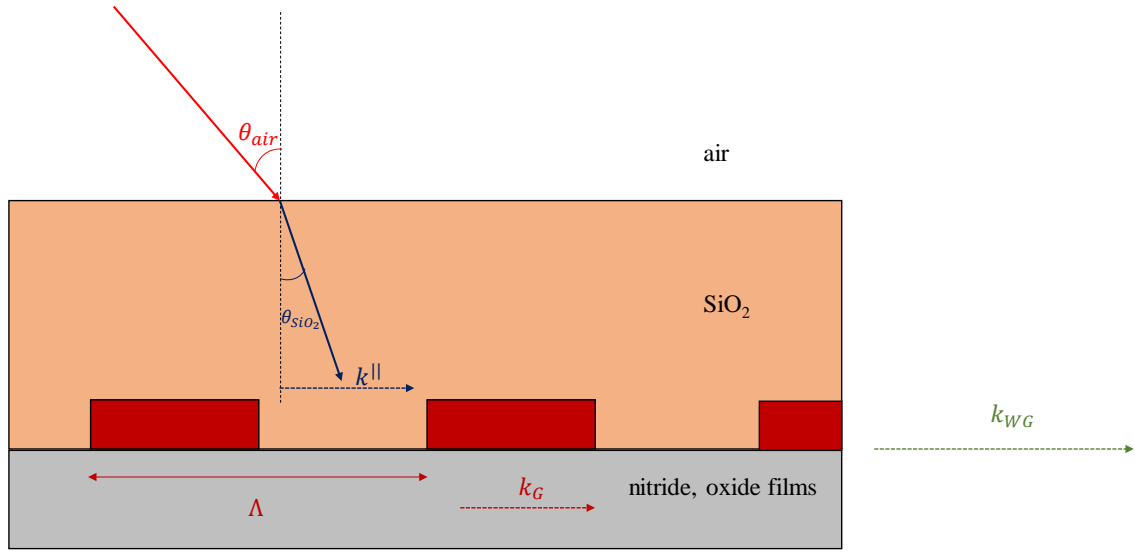
In our setup, the incident angle of the fibers was controlled by the fiber holders. As depicted in the figure below in red, the tip of the fiber was controlled by the fiber holder end. We had several available, with 10°, 15°, 30° and 40° end angle. Moreover, there were two micrometers that allowed us to adjust the angle by  $\pm 5^\circ$  degrees.



In the figure below we can observe a side view (from the rear camera) of the system with a 30° holder.



From a theoretical perspective, we have to match the momentum of the wave and the momentum of the grating to the actual momentum of the waveguide.



The incident wave has a propagation constant  $\vec{k}$ . Since we are only interested in the horizontal direction, we will only focus on the parallel component to the grating, that is found multiplying by the sine:

$$k_{||} = k_0 \cdot \sin(\theta_{SiO_2}) \cdot n_{eff_{SiO_2}} \quad (6.29)$$

For Snell's law, we can simplify the expression of the parallel component of the parallel wave:

$$n_{eff_{air}} \cdot \sin(\theta_{air}) = n_{eff_{SiO_2}} \cdot \sin(\theta_{SiO_2}) \quad (6.30)$$

Therefore, we can rewrite the expression, knowing that  $n_{eff_{air}} \approx 1$ , where  $\theta = \theta_{air}$ , the angle of the incident wave in the air:

$$k_{||} = k_0 \cdot \sin \theta \quad (6.31)$$

The momentum added by the grating coupler to the wave can be written as

$$k_G = \frac{2\pi}{\Lambda} \quad (6.32)$$

Where  $\Lambda$  is the period of the grating coupler. The momentum of the waveguide can be expressed as

$$k_{WG} = k_0 \cdot n_{eff_{WG}} \quad (6.33)$$



The  $n_{eff_{WG}}$  is the effective index of the waveguide. In this case we should see the input waveguide as the grating coupler, and this is the momentum we want to match. A grating coupler is a periodic structure of, on one part silicon and on the other part a combination of nitrides and oxides. Therefore,  $n_{eff_{WG}}$  is the combination of the effective index of silicon averaged to the effective index of the spaces where there is no silicon, so a combination of nitride and oxide films.

Thus, since we already have all the data, the matching can be understood as:

$$k_{||} + k_G = k_{WG} \quad (6.34)$$

$$k_0 \cdot \sin \theta + \frac{2\pi}{\Lambda} = k_0 \cdot n_{eff_{WG}} \quad (6.35)$$

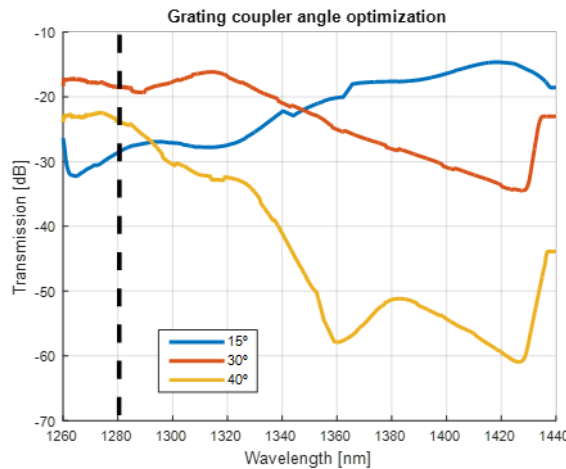
$$\frac{2\pi}{\lambda} \cdot \sin \theta + \frac{2\pi}{\Lambda} = \frac{2\pi}{\lambda} \cdot n_{eff_{WG}} \quad (6.36)$$

$$\sin \theta = n_{eff_{WG}} - \frac{\lambda}{\Lambda} \quad (6.37)$$

We have to note that  $n_{eff_{WG}}$  is wavelength dependent, so it makes the relationship a little bit more complicated. At wavelengths around 1280 nm,  $n_{eff_{WG}} \approx 2$ . The period of the grating coupler we are using is  $\Lambda = 1 \mu\text{m}$ .

From this equation, we can extract that the optimum angle for working at  $\lambda = 1280 \text{ nm}$  is  $\theta = 45$  degrees.

Talking about experimental results, we have observed that the holder that best suits to the wavelength we are using, 1280 nm, is the 30° holder. The difference from the theory might come because we are using lensed fibers, that have their tip like a cone, therefore, the angle can be modified a bit. Using conventional fibers with their perpendicular end, the optimal holder was found to be the one at 40°.



The difference at 1280 nm is 5.6 dB with respect to 40° and 10.6 dB with respect to 15°.

# 7 References

---

- [1] Ho, R., Mai, K. W., & Horowitz, M. A. (2001). The future of wires. *Proceedings of the IEEE*, 89(4), 490-504.
- [2] Haurylau, M., Chen, G., Chen, H., Zhang, J., Nelson, N. A., Albonesi, D. H., ... & Fauchet, P. M. (2006). On-chip optical interconnect roadmap: challenges and critical directions. *IEEE Journal of Selected Topics in Quantum Electronics*, 12(6), 1699.
- [3] Vivien, L. (2015). Computer technology: Silicon chips lighten up. *Nature*, 528(7583), 483-484.
- [4] Chang, J., Chen, S. L., Chen, W., Chiu, S., Faber, R., Ganesan, R., ... & Rusu, S. (2009, June). A 45nm 24MB on-die L3 cache for the 8-core multi-threaded Xeon® Processor. In *2009 Symposium on VLSI Circuits* (pp. 152-153). IEEE.
- [5] Miller, D. (2010, July). Device Requirements for Optical Interconnects to CMOS Silicon Chips. In *Photonics in Switching* (p. PMB3). Optical Society of America.
- [6] Watts, M. R., Zortman, W. A., Trotter, D. C., Young, R. W., & Lentine, A. L. (2011). Vertical junction silicon microdisk modulators and switches. *Optics express*, 19(22), 21989-22003.
- [7] Timurdogan, E., Sorace-Agaskar, C. M., Sun, J., Hosseini, E. S., Biberman, A., & Watts, M. R. (2014). An ultralow power athermal silicon modulator. *Nature communications*, 5.
- [8] Xu, Q., Manipatruni, S., Schmidt, B., Shakya, J., & Lipson, M. (2007). 12.5 Gbit/s carrier-injection-based silicon micro-ring silicon modulators. *Optics express*, 15(2), 430-436.
- [9] Young, I. A., Mohammed, E., Liao, J. T., Kern, A. M., Palermo, S., Block, B. A., ... & Chang, P. L. (2010). Optical I/O technology for tera-scale computing. *IEEE Journal of solid-state circuits*, 45(1), 235-248.
- [10] Shainline, J. M., Orcutt, J. S., Wade, M. T., Nammari, K., Moss, B., Georgas, M., ... & Popović, M. A. (2013). Depletion-mode carrier-plasma optical modulator in zero-change advanced CMOS. *Optics letters*, 38(15), 2657-2659.
- [11] Alloatti, L., Cheian, D., & Ram, R. J. (2016). High-speed modulator with interleaved junctions in zero-change CMOS photonics. *Applied Physics Letters*, 108(13), 131101.

- [12] Sun, C., Wade, M. T., Lee, Y., Orcutt, J. S., Alloatti, L., Georgas, M. S., ... & Moss, B. R. (2015). Single-chip microprocessor that communicates directly using light. *Nature*, 528(7583), 534-538.
- [13] Alloatti, L., & Ram, R. J. (2016). Resonance-enhanced waveguide-coupled silicon-germanium detector. *Applied Physics Letters*, 108(7), 071105.
- [14] Green, W. M., Rooks, M. J., Sekaric, L., & Vlasov, Y. A. (2007). Ultra-compact, low RF power, 10 Gb/s silicon Mach-Zehnder modulator. *Optics express*, 15(25), 17106-17113.
- [15] Thomson, D. J., Gardes, F. Y., Fedeli, J. M., Zlatanovic, S., Hu, Y., Kuo, B. P. P., ... & Reed, G. T. (2012). 50-Gb/s silicon optical modulator. *IEEE Photonics Technology Letters*, 24(4), 234-236.
- [16] Rabus, D. G. (2007). Ring Resonators: Theory and Modeling. *Integrated Ring Resonators: The Compendium*, 3-40.
- [17] Soref, Richard A., & Bennett, Brian R. (1987). Electrooptical effects in silicon. *IEEE journal of quantum electronics*, 23(1), 123-129.
- [18] Alloatti, L., Srinivasan, S. A., Orcutt, J. S., & Ram, R. J. (2015). Waveguide-coupled detector in zero-change complementary metal–oxide–semiconductor. *Applied Physics Letters*, 107(4), 041104.
- [19] Cheian, D. (2016). T-Junction Resonant Modulators and Detectors in CMOS. *Master's Thesis*, Research Laboratory of Electronics, MIT.
- [20] Kim, Y., Takenaka, M., Osada, T., Hata, M., & Takagi, S. (2014). Strain-induced enhancement of plasma dispersion effect and free-carrier absorption in SiGe optical modulators. *Scientific reports*, 4.
- [21] Kim, Y., Fujikata, J., Takahashi, S., Takenaka, M., & Takagi, S. (2016). First demonstration of SiGe-based carrier-injection Mach-Zehnder modulator with enhanced plasma dispersion effect. *Optics express*, 24(3), 1979-1985.
- [22] Takenaka, M., & Takagi, S. (2012). Strain engineering of plasma dispersion effect for SiGe optical modulators. *IEEE Journal of Quantum Electronics*, 48(1), 8-16.
- [23] Van Zeghbroeck, B. J (1997). Effective mass in semiconductors. *Website available: <http://ecee.colorado.edu/~bart/book/effmass.htm>*
- [24] Cheian, D., Alloatti, L., & Ram, R. J. (2016, August). Optimization of high-speed CMOS optical modulators with interleaved junctions. In *Lester Eastman Conference (LEC), 2016* (pp. 1-3). IEEE.